7

PREPRINT UCRL-83149

Lawrence Livermore Laboratory

THEORY AND SIMULATION OF LASER PLASMA COUPLING

William L. Kruer

August 9, 1979

This paper was prepared for the submission to the 20th Scottish University Summer School in Physics, St. Andrews, Scotland. August 13-20, 1979

THEORY AND SIMULATION OF LASER PLASMA COUPLING*

W. L. Kruer

University of California, Lawrence Livermore Laboratory
Livermore, California 94550

Abstract

The coupling of intense laser light with plasmas is a topic of great interest. Collective processes play an important role in this coupling. In these lectures, we consider the theory and simulation of these processes, with particular emphasis on their nonlinear evolution. First a brief introduction to computer simulation of plasmas using particle codes is given. Then the absorption of light via the generation of plasma waves is considered, followed by a discussion of stimulated scattering of intense light. Finally these calculations are compared with experimental results.

*Work performed under the auspices of the U.S. Department of Energy by the Lawrence Livemore Laboratory under contract number W-7405-ENG-48.

The idea of using large, high-power lasers to compress and heat fusion fuel to thermonuclear conditions is basically very simple: a pulsed laser can focus energy onto a small target, compressing and heating the fuel inside to ignition conditions. The resulting plasma is confined by its own inertia long enough for thermonuclear reactions to take place. Computer calculations have indicated that significant target gains might be achieved, that is, the energy produced from fusion can greatly exceed the laser energy necessary to implode the target. A large international effort is under way to investigate the feasibility of laser fusion energy.

The coupling of intense laser light to targets is obviously one very important component of laser fusion studies. These lectures are intended to be a brief introduction to laser plasma coupling. The specific topics are chosen to be representative and to focus attention on some of the important nonlinear features of the coupling. In the first lecture, a brief introduction is given to plasma simulation using particle codes. In the second and third lectures, light absorption via the generation of plasma waves is examined. The fourth lecture is a discussion of stimulated scattering, a process whereby laser light is scattered from plasma waves. In the final lecture, calculations are briefly compared with experimental results. Throughout these lectures, the emphasis will be on a physical introduction to important concepts and nonlinear results, rather than on an exhaustive survey of the field.

LECTURE ONE: PLASMA SIMULATION USING PARTICLES CODES

INTRODUCTION

It is well known that a collisionless plasma will support waves (or collective modes of oscillation) and that such waves are often driven unstable. An understanding of the resulting plasma microturbulence can be very important for many practical applications, such as laser-induced pellet fusion or fusion via magnetic confinement. The turbulent state is sufficiently complex that the interpretation of experiments requires a good knowledge of what effects are produced by the many competing plasma nonlinearities. In general, analytic theory is not capable of describing the nonlinear behavior, except in a very weak turbulent regime. Such theory is extremely valuable but has a limited domain of applicability and is itself often intractable. Hence it has been essential to augment experiments and analytic theory by direct numerical simulation.

Particle codes have proven to be a very powerful tool for the numerical simulation of plasmas. In this first lecture, a brief and physical introduction to the concepts and techniques involved in such codes will be given. Then these concepts will be tested by comparing the results from a particle code with a numerical solution obtained by an independent and quite different approach (as well as with the results of an experiment). In subsequent lectures, several examples will be given of recent applications of particle codes to laser plasma interactions. These examples illustrate many of the strong points and limitations of such codes. The discussion will be aimed at a general technical audience and is intended to be an introduction rather than an exhaustive survey.

A PHYSICAL INTRODUCTION TO THE CONCEPTS AND TECHNIQUES

The use of a particle code is a very direct and fundamental way to follow the behavior of a collisionless plasma.[1-9] One simply considers a large collection of electrons and ions. As indicated schematically in Figure 1, the positions and velocities determine the charge and current densities. Maxwell's equations then give the electric and magnetic fields, allowing the positions and velocities to be updated according to Newton's laws. One continues around this basic cycle with a time step sufficiently small to resolve the fastest behavior in the problem, which is often the electron plasma frequency time scale. The electron plasma frequency is $\sqrt{\frac{4\pi ne^2}{m}}$, where n is the electron density.

Of course it is only practical to use a rather limited number of simulation particles and to calculate their behavior on a sufficiently coarse spatial grid. Fortunately a rather coarse computational grid is adequate. Due to the long range of the Coulomb force, the net force on a charge in a collisionless plasma is determined by the collective motion of the charges rather than by short-range, binary-type encounters. The resulting collective modes of oscillation (waves) have wavelengths which are typically $\gtrsim$ the electron (or sometimes the ion) Debye length ($\lambda_{De} = \sqrt{\frac{\theta_e}{4\pi ne^2}}$, where θ_e is the electron temperature and n the electron density). Hence one can resolve the forces on a computational grid whose spacing is of order the Debye length rather than the typical inter-particle spacing.

The basic techniques are best illustrated by discussing a one-dimensional, electrostatic particle code. (In the electrostatic limit, the magnetic field generated by plasma currents is negligible, and Maxwell's equations reduce to Poisson's equation, $\nabla \cdot E = 4\pi\rho$.) There are several different schemes commonly used to map the particles onto the spatial grid. Consider a particle with charge q located a distance ξ to the right of its nearest grid point (labeled i). In the NGP scheme, one simply assigns the charge of the particle to that nearest grid point; i.e., $\rho(i) = q$. It is more common to linearly interpolate the charge of the particle to its neighboring grid points; i.e., $\rho(i) = q(1-\xi)$ and $\rho(i+1) = q\xi$, where the cell size $\delta = 1$. In this so-called PIC or CIC scheme, the charge density is mapped onto the spatial grid correctly to dipole order.

One next solves for the electric field due to this charge density. This can be done by a direct finite differencing of Poisson's equation or by Fourier transforms. Due to the existence of the fast Fourier transform algorithm, the two approaches are generally competitive in speed. It is theoretically appealing to work in terms of Fourier components, but complicated boundary conditions are more easily incorporated when the finite-difference approach is used.

Finally, the electric field is mapped from the grid to the particles by a scheme consistent with that used in assigning the charge density. For example, in the (PIC, CIC) scheme, the electric field is linearly interpolated to the particle position. In the previous example, the force on the particles is then $q\,[(1-\xi)\,E(i) + \xi E(i+1)]$. The velocities and positions are updated by a standard leap-frog algorithm. By defining the position and velocity one-half time step apart, one in effect achieves second order accuracy in the time step with a minimum number of operations, as can be readily confirmed by performing a Taylor-expansion.

From a computational viewpoint, a particle code is clearly rather straightforward. Not surprisingly, numerical instabilities are rarely a problem. One noteworthy instability is associated with the aliasing introduced by the spatial grid.[10] Aliasing arises from the fact that one cannot distinguish a disturbance with wave vector k from one with wave vector $k + \frac{2\pi n}{\delta}$, where δ is the grid spacing and n an integer. A heuristic argument can be given. One can avoid this problem by ensuring that the aliased modes have a phase velocity less than the thermal velocity of the particles; i.e. $(k + \frac{2\pi n}{\delta})\ \lambda_{De} \gtrsim 1$, $n \neq 0$. Since the modes we wish to describe have $k\lambda_{De} < 1$, this gives the condition that $\frac{2\pi\lambda_{De}}{\delta} \gtrsim 2$, or $\lambda_{De} \gtrsim \frac{\delta}{\pi}$. In other words, one cannot describe too many Debye lengths with a single cell.

Of course, particle codes become somewhat more complex when the full set of Maxwell's equations is allowed and magnetic forces operate on the particles. But the basic concepts are the same: the use of a spatial grid whose spacing is chosen to resolve the collective behavior and the mapping between that discrete grid and the particles. A very appealing physical interpretation of these procedures can be given in terms of finite-size particles.[7] A particle of finite spatial extent does not support fluctuations over distances much less than its size (a). This provides a natural suppression of the short-wavelength fluctuations associated with collisional effects. Yet the behavior of a collection of extended particles exhibits the same long-wavelength ($\lambda >> a$) behavior as do point particles (with minor modifications of the dispersive properties of the waves). Furthermore, the mapping of such particles onto the spatial grid proceeds in a natural and systematic way as a Taylor expansion about the grid location nearest to the center of the extended charge.

Again it is instructive to consider a simple one-dimensional example. The charge density due to a collection of Gaussian-shaped charges is

$$\rho(x) = \frac{q}{\sqrt{2\pi}a} \sum_j \exp\left[-\frac{(x - x_j)^2}{2a^2}\right] \quad ,$$

where x_j is the center of the j^{th} charge and a is its half-width. A Fourier transform yields

$$\rho_k = q\, e^{-\frac{k^2a^2}{2}} \sum_j e^{-ikx_j} \quad ,$$

which is identical to the result for a collection of point particles except for a form factor $(e^{-k^2a^2/2})$. This form factor explicitly shows that fluctuations with wavelengths $\lambda \lesssim a$ are suppressed, whereas long wavelength ones ($\lambda >> a$) are relatively unaffected by the particle size.

To introduce the spatial grid, one expresses x_j in terms of the nearest grid point location plus a displacement,

$$x_j = n_j\delta + \Delta x_j$$

and expands the exponential assuming $\delta << a$. This yields $\rho_k = q e^{\frac{-k^2a^2}{2}} \sum_j e^{-ikn_j\delta} \sum_\ell (-ik\Delta x_j)^\ell/\ell!$. Note that the summation over ℓ is a summation over the multipole moments of each extended charge with respect to its nearest grid location. Truncating the multipole expansion at the dipole order and rearranging the sum over j, one obtains

$$\rho_k = e^{\frac{-k^2a^2}{2}} \text{ FT } [N(n) - ik\Delta R(n)].$$

FT denotes a Fourier transform and N(n) and ΔR(n) are the net monopole and dipole charge associated with each grid point; i.e.,

$$N(n) = \sum_{j\epsilon n} q$$
$$\Delta R(n) = \sum_{j\epsilon n} q\Delta x_j \ .$$

Physically one has replaced each extended charge by an extended charge plus an extended dipole located at its nearest grid point. The (PIC, CIC) scheme previously mentioned is in these terms an expansion to dipole order.

A similar multipole expansion can be used to determine the force on an extended charge. The net force is then expressed as the monopole charge times the electric field plus the dipole charge times the derivative of the field. Since the general procedure has been illustrated, no further details will be given.

COMPARISON WITH AN INDEPENDENT TECHNIQUE

These concepts are plausible, but how well do they work in practice? Can one describe the behavior of a collisionless plasma using a practical number of particles, which inevitably is far fewer than nature uses? It is well known that the Vlasov equation can be used to describe a plasma in the collisionless limit; i.e., when the number of particles per Debye sphere ($n\lambda_{De}^3$) is infinite. Hence a good check on the results of a particle code is to compare them with direct numerical solutions of this equation. Such comparisons[11] have indeed been carried out for a number of different nonlinear problems, establishing good agreement between the results from a particle code and from the Vlasov equation.

As an example, consider the nonlinear behavior of a large amplitude electron plasma oscillation on a time scale for which ion motion can be neglected. In a one-dimensional, electrostatic limit the Vlasov equation becomes

$$\frac{\partial f}{\partial t} + v\frac{\partial f}{\partial x} - \frac{e}{m} E \frac{\partial f}{\partial v} = 0.$$

$f(x,v,t)$ is the phase space distribution function of the electrons, and E is the electric field determined from Poisson's equation:

$$\frac{\partial E}{\partial x} = -4\pi e\left[\int f dv - n_0\right] ,$$

where n_0 is the uniform background ion density. The numerical solution of these equations was carried out by Fourier expanding the distribution function in both position and velocity space, and then solving the coupled equations for the Fourier components by the method of characteristics.

Figure 2 shows the computed evolution of the wave energy in both the large amplitude plasma wave and its lower sideband (the lower wavenumber and frequency plasma waves). The open symbols denote the solution of the Vlasov equation, and the solid symbols denote the results from a particle code (with 80,000 particles). The large plasma wave exhibits oscillations in energy due to the bouncing of electrons in the potential troughs associated with the wave. Simultaneously the lower sidebands exponentiate in energy, denoting what has been called a trapped particle instability.[12] From a computational viewpoint, this is quite a difficult problem, since one must follow both sizeable variations in the energy of the large wave and the concomitant growth of nearby waves over many orders of magnitude from the noise. Even so, the Vlasov and particle code results are in quite good agreement. It should be noted that these computational results are also in substantial agreement with experiment.[13] Figure 3 shows the experimentally measured evolution of the energy in a large plasma wave and in its lower sidebands. The large plasma wave was launched from a probe, and then its behavior monitored as a function of distance. (Hence this is the spatial analogue of the temporal problem considered in the simulations.) The simulations correctly describe both the main wave oscillations and the sideband growth. This example is a good illustration of how experiment, theory, and numerical simulation can mutually interact to clarify the nonlinear behavior of plasmas.

STATE OF THE ART OF PARTICLE CODES

Particle codes have been developed to a high level of sophistication and have been used to study numerous problems throughout plasma physics. Figure 4 shows a schematic of a state-of-the-art computer simulation[14] which is a good indication of the current capability of particle codes. One uses a 2-D electromagnetic, relativistic particle code and propagates laser light from a vacuum into an inhomogeneous plasma slab. The plasma response is followed not only along the electric field vector of the laser light but also along its direction of propagation. Such simulations have allowed the study of light absorption both via instabilities and via direct resonant excitation of plasma waves.

Although an invaluable tool, these 2-D simulations are a good example of some practical limitations in the use of particle codes. One is fairly restricted in both the size of plasma which can be simulated and the length of time for which the behavior can be followed. This can be illustrated by some simple estimates based on using a CDC 7600 computer. The largest practical spatial grid is composed of 40.000 grid points, since there are at least six arrays defined on this grid in the 2-D code. A single cell is used to describe no more than 2-3 λ_{De} (electron Debye lengths) in order to avoid the grid instabilities previously mentioned. Hence the simulated plasma can have a maximum size of ~400 λ_{De} by 400 λ_{De}, although of course the system need not be square. For typical laser plasma parameters, the size of the simulated plasma is then ~ $6\lambda_o$ by $6\lambda_o$, where λ_o is the laser light wavelength. As compared to an experiment, this is a small region of plasma.

Furthermore, to maintain minimal particle statistics (and hence noise levels), one uses at least 5-10 particles per Debye square, which translates to ~10^6 simulation particles for this large problem. A reasonably fast 2-D relativistic particle mover using the electromagnetic fields takes ~25 μsec/particle. Hence a computer simulation of 2500 time steps consumes about 20 hours of computer time. Since a typical time step is .2 ω_{pe}^{-1}, the total time simulated is ~500 ω_{pe}^{-1} or 100 laser light periods, again much shorter than experimental time scales. Of course, one can usually isolate the important physical mechanisms in much smaller systems, and can often improve the speed by [illegible] programming, but these numbers give some idea of the pratical limitations.

A particle code follows the micro-turbulent behavior of a plasma, that is, the turbulence on a short time and space scale. Not surprisingly, such fine scale calculations can be carried out for only small volumes of plasmas and short times. One generally uses particle codes to determine how microturbulence affects the local plasma properties such as energy absorption rates and transport coefficients. This information is then input either into theory and/or hydrodynamic-type codes in order to determine the global behavior of the system.

In conclusion, particle codes are a powerful and often indispensable tool to study strong plasma turbulence. The detailed diagnostics from the simulations often allow one to isolate and parameterize the important nonlinear effects. However, such codes of course operate on short time and space scales. Their results generally serve as an input to theory and to hydrodynamic codes.

LECTURE TWO: LASER PLASMA HEATING - PARAMETRIC INSTABILITIES

INTRODUCTION

One of the central questions in laser fusion studies concerns the mechanisms by which laser light is absorbed by a plasma. Since a hot plasma becomes collisionless, classical joule heating is usually insufficient unless very short wavelength or low intensity laser light is used. Fortunately one can heat even a collisionless plasma. This "anomalous absorption" arises since intense laser light excites plasma waves (or charge density fluctuations). The electric fields associated with such charge fluctuations in turn accelerate and heat the plasma particles.

A crude estimate of the efficiency of classical joule heating can be given. Physically this heating occurs because electron-ion collisions convert the coherent energy of oscillation of electrons in the electric field of the light wave into random thermal energy. It is easy to show that the energy damping rate of a light wave then is[15] $= \nu_{ei}\omega_{pe}^2/\omega_0^2$ where ν_{ei} is an electron-ion collision frequency: $\nu_{ei} = 3 \times 10^{-6} n_i Z^2 \ln\Lambda / T_{ev}^{3/2}$. Here n_i is the ion density, Z the ionization state, ω_{pe} the plasma frequency, ω_0 the light frequency, and T_{ev} the electron temperature in ev. As a simple example, for 1.06 μ laser light in a plasma with $T_{ev} = 10^3$ and Z = 3, the classical absorption length near the critical density is about 100 [illegible]. As the plasma heats, this absorption length becomes even longer (as [illegible]

[illegible] Hence collective heating (via plasma waves) is often the major source of laser light absorption.

The basic mechanism for the excitation of plasma waves is the oscillation of electrons by the electric field of the light across a variation in plasma density. This drives a charge density fluctuation which is

$$\delta n_e(x + x_{os}) - n_e(x) \approx x_{os} \cdot \nabla n_e \quad ,$$

where $x_{os} = eE_L/m\omega_o^2$. It is apparent that, if $\omega_o \approx \omega_{pe}$ (that is, if the laser light frequency is properly matched to the electron plasma frequency), electron plasma waves are resonantly driven. The variation in density can be due to the overall density gradient due to plasma expansion (this leads to resonance absorption, which will be discussed in the next lecture) or to the density fluctuations associated with other plasma waves, such as ion acoustic waves. Parametric instabilities near the critical density are a simple example of this latter effect.

In order to understand why such instabilities occur, we need only introduce one other concept: the ponderomotive force. The basic idea is very simple: there is a force due to a gradient in electric field intensity just as there's a force due to a gradient in plasma pressure. By using the two-fluid equations to describe the plasma response to an high frequency electric field, with amplitude E(x), it is readily shown that $F_p = -\omega_{pe}^2/\omega_o^2 \, \underline{\nabla} < E^2(x)/8\pi >$ where the brackets denote a time average over the high frequency oscillations.

The feedback loop leading to instability is illustrated in Fig. 5. Consider a (thermal level) small density fluctuation associated with an ion acoustic wave. The light field (E_L) couples with the density fluctuation (δn) to drive a high frequency electric field (E_p) associated with an electron plasma wave ($E_L \delta n \rightarrow E_p$). In turn, this plasma field couples with the light wave field to produce a fluctuation in field pressure which enhances the density fluctuation ($E_L E_p \rightarrow \delta n$). Hence instability is possible, in this case leading to exponential growth of both electron plasma waves and ion accoustic waves provided $\omega_0 \approx \omega_{pe} + \omega_{ia}$. This is called the ion acoustic instability. There is also another branch of instability in which the ion density fluctuation is not a "normal mode" of the undriven plasma but rather a zero-frequency, purely growing mode. This is called the oscillating two-stream instability. Both branches of instability are readily derived[16] from the coupled wave equations for the high and low frequency waves. In this second lecture, we will now briefly consider a simple and instructive example of the nonlinear evolution of these instabilities.

NONLINEAR EVOLUTION OF PARAMETRIC INSTABILITIES

In order to focus on the nonlinear evolution, we consider the simplest model problem: a plasma with uniform density which is driven by an imposed spatially-independent pump field ($E_0 \sin\omega_0 t$) with a frequency (ω_0) near the electron plasma frequency. Such a pump field models the electric field of a light wave near its critical density under the assumption that the wave number of the light wave is negligible compared with the wave numbers of the plasma waves which are excited. Since the unstable plasma waves preferentially grow along the electric vector of the pump field, a great deal can be learned by using a one-dimensional electrostatic particle code.

A few simple results from a sample simulation[17] illustrate important features of the collective heating. In this example, $\omega_0 = 1.04\,\omega_{pe}$, $eE/m\omega_{pe} = 0.5v_e$ (the electron thermal velocity), and the ion-electron mass ratio is 100, which is sufficient to clearly separate the electron and ion time scales. Figure 6a shows the evolution of the energy in plasma waves, and Fig. 6b shows the evolution of the kinetic energy of the simulated plasma. At first there is essentially no plasma heating, reflecting the fact that the plasma is nearly collisionless. Meanwhile the plasma waves are exponentiating in amplitude. Finally these waves saturate, concomitant with the onset of rapid plasma heating due to an acceleration of plasma particles by the large amplitude plasma waves. An effective collision frequency corresponding to this anomalous heating is very large, $\nu^* \approx 0.06\,\omega_0$, where ν^* describes the rate at which the plasma energy increases with time in the nonlinear state.

Another particularly important feature of the anomalous heating was first discovered in the computer simulations. Figure 7 shows a typical heated electron velocity distribution calculated with the particle code. The heating has been principally a production of very high velocity tails on the distribution. This generation of very high velocity electrons takes place since large amplitude electron plasma waves readily accelerate particles out to their phase velocity. As shown in Fig. 8, the generation of such nonthermal distributions have been confirmed in a laboratory experiment on microwave heating of a low-density plasma.[18]

The physics of the nonlinear saturation can be very rich. There are a number of different regimes depending on the pump field intensity. When the plasma is strongly driven ($eE_0/m\omega_{pe}v_e \gtrsim 1$), the dominant process is simply electron trapping in the most unstable plasma wave. Trapping occurs when electrons are nonlinearly brought into resonance with the wave. A large energy transfer then occurs, as the electrons are efficiently accelerated by the wave. In a cold plasma, this obviously occurs when the velocity of oscillation of an electron in the wave ($v_w = eE/m\omega_{pe}$) becomes equal to its phase velocity (v_p). In a warm plasma, trapping occurs at a significantly smaller amplitude for several reasons. Faster electrons are more easily brought in resonance, and the sizeable pressure force associated the density fluctuation of the wave gives an additional acceleration.

We can crudely model the effect of temperature on electron trapping by considering a waterbag model, which corresponds to replacing a Maxwellian distribution with a velocity distribution which is constant between $\pm\sqrt{3}v_e$. In this description which assumes fixed ions, the average density (n) and velocity (u) satisfy the same equations as those for a warm electron fluid:[19]

$$\frac{\partial n}{\partial t} + \frac{\partial}{\partial x} nu = 0$$

$$\frac{\partial n}{\partial t} + u\frac{\partial u}{\partial x} = \frac{-e}{m}E - \frac{1}{mn}\frac{\partial p}{\partial x} \quad , \qquad \text{II-1}$$

where p/n^3 is a constant. Introducing $E = -\partial\phi/\partial x$ and transforming to the wave frame with velocity v_p gives

$$nu = n_0 v_p \quad ,$$

$$u^2 - \frac{2e\phi}{m} + 3v_e^2 \left(\frac{n}{n_0}\right)^2 = v_p^2 + 3v_e^2 \; . \qquad \text{II-2}$$

Here n_0 is the density of the uniform, unperturbed plasma. Hence

$$\frac{2e\phi}{mv_p^2} = \frac{u^2}{v_p^2} - 1 - \beta + \beta \left(\frac{v_p^2}{u^2}\right) \quad . \qquad \text{II-3}$$

where $\beta = 3v_e^2/v_p^2$. By differentiating with respect to u, it is easy to see that ϕ has an extremum (ϕ_{cr}) when $u/v_p = \sqrt[4]{\beta}$. The corresponding potential is

$$-\frac{2e\phi_{cr}}{mv_p^2} = (1 - \sqrt{\beta})^2 \quad . \qquad \text{II-4}$$

This simply corresponds to the condition that the net energy of the fastest electron be zero in the wave frame.

To determine the critical value of the electric field, we consider Poisson's equation:

$$\frac{\partial^2\phi}{\partial x^2} = 4\pi e(n-n_0) \quad .$$

Multiplying by $\partial\phi/\partial x$ and using equation II-1 gives (in the wave frame)

$$\frac{\dot{\phi}^2}{2} + 4\pi \left[n_0 e\phi - mnu^2 - n_0 m v_e^2 \left(\frac{n}{n_0}\right)^3\right] = \qquad \text{II-5}$$

$$-2\pi n_o m v_p^2 \left[(1-\sqrt{\beta})^2 + 8/3\sqrt[4]{\beta}\right] \quad .$$

The constant has been evaluated by noting that $\dot{\phi} = 0$ when $\phi = \phi_{cr}$. The maximum electric field obtains when $\phi = 0$;

$$\frac{\dot{\phi}^2_{max}}{4\pi n_o m v_p^2} = 1 + 2\sqrt{\beta} - 8/3\,\sqrt[4]{\beta} - \beta/3 \quad . \qquad \text{II-6}$$

Let us now use this result to estimate the saturation in the simulations, considering an example in the trapping regime: $eE_o/m\omega_o v_e = 1.0$ and $\omega_o = 1.04\,\omega_{pe}$. Linear theory applied to this case predicts that the most unstable plasma wave has a wavenumber $k \approx 0.25\,\omega_{pe}/v_e$ for the electron-ion mass ratio of 0.01 used in this simulation. Equation II-6 then predicts that trapping onsets when $eE/m\omega_{pe}v_e \approx 0.8$, which compares reasonably well with the computed value of $eE/m\omega_{pe}v_e \approx 0.6$ at saturation.

A simple estimate of the anomalous heating rate can also be given. The instability theory allows us to estimate the energy transfer from the external driver to the electron plasma oscillations as $2\gamma\langle E_w^2/4\pi\rangle$ where γ is the growth rate and $\langle E_w^2\rangle/4\pi$ is the energy associated with the plasma oscillations. The transfer of energy to the particles is given by our definition of the anomalous heating rate as $\nu^* E_o^2/8\pi$. When the plasma oscillations saturate, these energy flows balance. Hence, we estimate ν^* as

$$\nu^* \simeq 4\gamma\,(\langle E_w^2\rangle/E_o^2) \quad , \qquad \text{II-7}$$

where $\langle E_w^2\rangle$ is the mean square electric field at saturation. For the example discussed above, Eq. II-7 predicts $\nu^* \approx 0.04\ \omega_{pe}$, which again compares reasonably well with the computed value of $\nu^* \approx 0.06\ \omega_{pe}$.

There are many other nonlinear regimes.[20] A particularly interesting one obtains when $eE_0/m\omega_{pe}v_e \ll 1$. Then the excited plasma waves obtain an amplitude $E \sim E_0$ without trapping. Hence they in turn act like efficient "pumps" to drive other plasma waves unstable, and so on. The net result is a cascade (collapse) of energy from long wavelength waves to short wavelength ones which Landau damp. Again the saturated state is characterized by a steady transfer of energy from the pump field to plasma waves to a heated tail of electrons.

LECTURE THREE: RESONANCE ABSORPTION OF INTENSE LASER LIGHT

INTRODUCTION AND LINEAR THEORY

In this third lecture we will consider resonance absorption. In an inhomogeneous plasma, electrostatic waves are generated whenever light has a component of its electric vector along the direction of the density gradient. Energy flows from the light wave into an electrostatic wave which then heats the electrons. First we will give a physical model for resonant coupling into a plasma wave and then show how an obliquely incident light wave can provide the coupling. This simple treatment is sufficient to both elucidate the physics and to exhibit the important dependences of resonance absorption. Finally we will discuss the nonlinear evolution of resonance absorption as illustrated in computer simulations.

To investigate the resonant coupling,[21] consider a one dimensional capacitor problem: a nonuniform plasma externally driven by a spatially uniform electric field with amplitude E_d and frequency ω_0. From Maxwell's equations we have

$$\frac{\partial E}{\partial t} + 4\pi J = \left\langle \frac{\partial E}{\partial t} + 4\pi J \right\rangle \qquad \text{III-1}$$

where E is the electrostatic field. J is the current density and the brackets denote the spatially independent component. If we neglect ion motion and linearize. the current density is

$$J = -en_o(z)v \quad . \qquad \text{III-2}$$

Here v is the oscillation velocity of electrons in both the imposed field ($E_d \cos \omega_o t$) and the self-consistent field (E) due to the plasma. Taking time derivatives of equations (III-1) and (III-2) and using the linearized equation of motion, we then obtain

$$\frac{\partial^2 E}{\partial t^2} + \omega_{pe}^2(z)E + \nu_{ei}\frac{\partial E}{\partial t} = -\left[\omega_{pe}^2(z) - <\omega_{pe}^2(z)>\right] E_d \cos \omega_o t. \qquad \text{III-3}$$

Taking $E \sim e^{i\omega_o t}$, assuming a linear density profile, and solving for the driven response gives

$$E = \frac{\omega_{pe}^2(z)E_d}{\omega_o^2 - \omega_{pe}^2(z) + i\nu_{ei}\omega_o} \quad . \qquad \text{III-4}$$

Note the resonant response when $\omega_o \approx \omega_{pe}$.

The flux of energy (I_{ABS}) which must be supplied by the externally imposed driver field is now readily obtained by computing the energy lost by the pump field:

$$I_{ABS} = \int \nu_{ei} \frac{|E|^2}{8\pi} dx \quad .$$

If we again assume a linear density gradient ($n = n_{cr}\, z/L$),

$$I_{ABS} = \frac{\omega_o L E_d^2}{8} \quad . \qquad \text{III-5}$$

Note that ν_{ei} cancels out, and so the energy flow is independent of the detailed mechanism which provides the damping of the electrostatic field. Physically the height of the resonance is $\alpha\ 1/\nu_{ei}$ and the width of the resonance is $\alpha\nu_{ei}$; hence the cancellation.

Equations (III-4) and (III-5) show that whenever a driver field oscillates electrons across a density gradient, an electrostatic oscillation is resonantly driven near the critical density (i.e., where $\omega_o = \omega_{pe}$). Such a driver field is provided by a light wave obliquely incident onto an inhomogeneous plasma if a component of its electric field vector is along the direction of the density gradient.

Consider now a light wave obliquely incident onto an inhomogeneous plasma slab. As shown in Fig. 9, we take the propagation k vector of the wave to be in the y-z plane (without loss of generality), the density gradient to be in the z direction, and the angle between ∇n and k in vacuum to be Θ. Since the density is only a function of z, k_y is conserved and so equals $\omega_o/c \cos \Theta$. The dispersion relation for the light wave then becomes

$$\omega_o^2 = \omega_{pe}^2 + \omega_o^2 \sin^2 \Theta + k_z^2 c^2 \quad . \qquad \text{III-6}$$

The maximum density which the wave reaches (n_t) is given by the cutoff condition $k_z = 0$:

$$n_t = n_{cr} \cos^2 \Theta \quad . \qquad \text{III-7}$$

Note that the wave reflects below the critical density, although of course the fields do penetrate roughly a few skin depths into the higher density region.

The occurrence of resonance absorption depends on the orientation of the electric vector ($\underline{E}_L$) of the light. If $\underline{E}_L$ is in the x-direction (i.e., out of the plane of incidence which is the plane defined by $\underline{\nabla}n$ and $\underline{k}$), the electric field has no component along the density gradient and so does not excite the resonance. This is called s-polarized light. If $\underline{E}_L$ is in the plane of incidence (i.e., in the y-z plane), it does have a component along the density gradient. This is called p-polarized light. Although the obliquely incident light reflects at a density lower than critical, its fields will still tunnel to the critical density region and so excite the resonance.

A very simple estimate can be given for the resonance absorption of p-polarized light. Basically we need only to estimate the component of the electric field which drives the resonance (E_d) and then use equation III-5. To do this it is most convenient to work in terms of the magnetic field of the light wave. If we assume p-polarized light and the geometry depicted in Fig. 9,

$$\underline{B} = \hat{x}B(z)\ \exp(-i\omega t + i\omega_0 y\ \sin\Theta/c).$$

From Ampere's law we then obtain

$$E_z = \frac{\sin\ \Theta\ B(z)}{\epsilon\ (z)} \quad , \tag{III-8}$$

where ϵ is the dielectric function of the plasma. By analogy to equation III-4,

$$E_d = \sin\Theta\, B(n = n_{cr}) \quad . \qquad \text{III-9}$$

The magnetic field at the critical density $[B(n = n_{cr})]$ can be simply estimated as its value at the turning point density times the exponential decay of the field into the critical density region. If we assume a linear density ramp and then use the well-known Airy function solution for light propagation in a linear profile,

$$B(n = n_{cr}) \simeq \frac{.92E_{FS}}{\left(\frac{\omega_0 L}{c}\right)^{1/6}} \exp\left(-2/3\, \omega_0 L/c \sin^3\Theta\right) \quad , \qquad \text{III-10}$$

where E_{FS} is the free-space value of the electric field of the light. The $(k_0L)^{1/6}$ term comes from the decrease of the magnetic field from its free space value as the group velocity of the wave becomes small. Inserting equation III-10 into equation III-9 then gives

$$E_d \simeq \frac{.92E_{FS}}{\left(\frac{\omega_0 L}{c}\right)^{1/6}} \sin\Theta \exp\left(-2/3\, \omega_0 L/c \sin^3\Theta\right) \quad . \qquad \text{III-11}$$

The absorption is now readily estimated using equation III-11 in equation III-5. Noting that $I_{ABS} = f\, cE_{FS}^2/8$, and defining $\tau = (k_0L)^{1/3} \sin\Theta$ gives

$$f \simeq \frac{\phi^2(\tau)}{2} \quad ,$$

where f is the fractional absorption and

$$\phi(\tau) \simeq 2.31\, \tau \exp\left(-2/3\, \tau^3\right) \qquad \text{III-12}$$

The important features of resonance absorption can be deduced from the function ϕ [illegible], which is plotted in fig. 10. Note that the absorption, which is equal to ϕ^2 [illegible]/2, vanishes at [illegible] = 0 (no component of the electric field along the direction of the density gradient). The absorption is very small for large angles such that [illegible] the fields have to tunnel through too large a distance). Maximum absorption occurs for an angle [illegible]$_{MAX}$, defined by [illegible] 0.8, and the range of angles for which the absorption is sizeable is [illegible]$_{MAX}$. [illegible] the significance of resonance absorptin depends strongly on the value of the density gradient length near the critical density. If [illegible] is very large, this absorption is effective for only a narrow range of angles. If [illegible]$_0L/c \lesssim 10$, resonance absorption occurs for a [illegible] range of angles. The optimum absorption in a linear profile is somewhat over-estimated by this simple model and is actually 0.5, rather than 0.85.

COMPUTER SIMULATIONS OF RESONANCE ABSORPTION

Even though the basic process is linear, nonlinear effects play a central role in resonance absorption of intense laser light. Nonlinear effects determine the self-consistent density gradient length, the size of the resonantly-generated fields, and the heated electron distributions. To explore these nonlinear aspects, we again turn to computer simulations.[23-26]

These simulations[24] are carried out with a two-dimensional code which solves the complete set of Maxwell's equations and includes relativistic particle dynamics. Plane light waves are propagated from vacuum into an inhomogeneous slab of plasma. Variations are followed both along the propagation vector of the light and along its electric vector, which allows for resonance absorption and for the generation of parametric instabilities. Reflected light waves are allowed to freely pass out of the system. Particle boundary conditions are chosen to model a freely expanding plasma adjacent to a reservoir of constant temperature plasma. The initial density varies with x (the direction normal to the slab) from zero to a supercritical value. A region of vacuum is included adjacent to the low density boundary to allow for free expansion of the plasma. Particles impinging on the high density boundary are replaced with equal incoming flux distributed according to $v_x f_m(v)$, where v_x is the component of the velocity normal to the boundary and $f_m(v)$ is the initial Maxwellian velocity distribution. The plasma evolution is followed until a quasi-steady state has been established.

A typical simulation will again illustrate the principal effects. In this example, p-polarized light is incident at an angle of 24^0 onto an initial density profile which rises linearly from 0 to 1.7 n_{cr} in a distance of $3\lambda_0$ (where λ_0 is the free space wavelengths). The free space amplitude of the electric field of the light is $eE/m\omega_0 c$ = 0.09, which corresponds to an intensity of $I\lambda_0^2 \approx 10^{16}$ W μ^2/cm^2. The initial electron temperature is 4 keV, and the ion-electron mass ratio is 100.

After the light wave penetrates to its turning point, an electrostatic field is resonantly excited at the critical density. The magnitude of this field initially grows linearly in time, becoming more [illegible] localized to the critical density surface as expected from [illegible] III-3. Finally the resonantly-driven field becomes [illegible] intense and localized that electrons can be accelerated [illegible] in one oscillation period, a process called wavebreaking. When [illegible] condition is satisfied, electrons which enter the oscillating [illegible] the proper phase are efficiently heated, taking energy from [illegible] and saturating its growth.

A simple model[27] can be used to estimate the size of the [illegible]-driven field at wavebreaking. We again consider a capacitor [illegible] an inhomogeneous plasma driven by an imposed field E_d sin [illegible] we assume a cold, one-dimensional plasma and fixed ions, the [illegible] evolution is readily described in terms of the Lagrangian variable $\xi(x_0)$, which is the displacement of an electron initially at position x_0. ⟷ Using Poisson's equation and the equation of motion, we obtain

$$\ddot{\xi} + \omega_{pe}^2(x_0)\,\xi = \frac{eE_d}{m}\sin\omega_0 t \quad . \qquad \text{III-13}$$

If we assume a linear density profile ($\omega_{pe}^2 = \omega_0^2 x_0/L$), the solutions for ξ and $\partial\xi/\partial x_0$ at the resonant point are trivial:

$$\xi = x_d\,\omega_0 t/2\,\cos\omega_0 t \quad , \qquad \text{III-14}$$

$$\partial\xi/\partial x_0 = -x_d/8L\,(\omega_0 t)^2\sin\omega_0 t \quad , \qquad \text{III-15}$$

where $x_d = eE_d/m\omega_0^2$ and it is assumed that $x_d/L << 1$.

Wavebreaking occurs when electrons cross one another ($\partial\xi/\partial x_0 = -1$), which happens when $\xi = \sqrt{2x_dL}$. Hence the amplitude of the resonantly-driven field at wave breaking is

$$eE/m\omega_0 = \sqrt{2eE_dL/m} \quad . \qquad \text{III-16}$$

More physically, we can think of wave breaking as simply electron trapping by the localized oscillating field. We first define the effective wave number of the driven wave as $k^* = 1/\partial\xi/\partial x_0$, where we of course mean the ratio of the amplitudes of these oscillating quantities. Using equations III-14 and III-15 then gives $k^* \approx 1/\sqrt{2Lx_d}$. Wave breaking occurs when the oscillation velocity of an electron in the resonantly-driven field ($v_w = \omega_0\xi$) equals the phase velocity of the wave ($v_p = \omega_0/k^*$). This condition again yields equation III-16.

We can now estimate the amplitude of the resonantly-driven field at saturation by using equation III-11 to relate E_d to the electric field of the incident laser light. For the parameters of the sample simulation, this cold plasma prediction becomes $eE/m\omega_0c = 0.47$, which compares reasonably well with the observed value of $eE/m\omega_0c \approx 0.3$. To obtain closer agreement, we must incorporate warm plama effects[28] which, of course, reduce the wave breaking ("trapping") amplitude as discussed in the previous lecture.

The feedback of these intense fields (and the concomitant localized heating) on the plasma density profile is a crucial feature of the long-time evolution of the coupling. The pronounced profile modification is demonstrated in Fig. 11, which shows three snapshots of the density profile as it evolves from its initial linear profile to a quasi-steady, very steepened profile. The ponderomotive force due to the intense, localized electrostatic field ejects plasma, digging a hole in the plasma density at the critical surface. The plasma ejected towards the vacuum expands away, leaving a locally steepened density profile which is supported by the pressure of both the localized electrostatic wave and the reflecting light wave.

This profile steepening has important consequences for the mix of absorption processes. In particular, resonance absorption becomes important for a wide range of angles of incidence. This is demonstrated in Fig. 12, which is a plot of the fractional absorption of p-polarized light (after the profile steepening) versus angle of incidence as computed in a series of simulations with the same initial plasma conditions as the sample simulation. Note that the absorption peaks at about 50% for a sizeable angle of incidence ($\theta_{max} \approx 24^{o}$) and is quite large over a broad range of angles ($\Delta\theta \sim \theta_{max}$). This is qualitatively as expected from our simple theoretical discussion of resonance absorption. In addition, parametric instabilities near the critical density (discussed in the previous lecture) are strongly limited, since there's a very small region of plasma in which these instabilities can operate. Note that the absorption is only about 15% for normally incident light.

Finally, the profile steepening strongly reduces the heated electron energies due to the resonantly-generated wave. At wavebreaking, a small fraction of the electrons (those entering the wave with the proper phases) are strongly heated to an effective temperature of order mv_w^2, where v_w is the oscillation velocity of an electron in the resonantly-driven wave ($v_w = eE/m\omega_0$). As is apparent from the simple model of wavebreaking, the resonantly-driven field decreases in amplitude as the profile steepens. Physically, the wave then has a smaller spatial extent which corresponds to a lower effective phase velocity. Hence it traps electrons at a lower amplitude and heats them to a lower energy.

LECTURE FOUR: STIMULATED SCATTERING OF INTENSE LASER LIGHT

INTRODUCTION

In this fourth lecture, we will focus on some of the plasma processes which can be significant when there's a sizeable region of plasma with density less than the critical density. In particular, these processes represent instabilities which can be thought of as the resonant decay of the incident light wave into two electron plasma waves (the two-plasmon decay instability[29]), into a scattered light wave plus an electron plasma wave (the Raman instability), or into a scattered light wave plus an ion acoustic wave (the Brillouin instability). These latter two instabilities[30] give rise to the possibility that the incident light will be scattered before it reaches the higher densities near the critical density where the absorptive processes are most efficient. In practice, this means that the laser plasma coupling may be considerably altered when an extensive region of underdense plasma is created either by use of a prepulse or a long pulse.

The Brillouin instability is potentially the most dangerous of these instabilities. As can be seen from the frequency matching conditions ($\omega_o = \omega_t + \omega_{ia}$, where ω_o is the frequency of the laser light, ω_t is the frequency of the scattered light wave, and ω_{ia} is the frequency of the ion wave), this instability is operative throughout the underdense plasma. In addition, by the Manley-Rowe relations, nearly all the energy of the incident light can be transferred to the scattered light wave since $\omega_{ia}/\omega_0 << 1$. Hence we will focus our attention on this instability. First we will briefly consider the linear theory and the effect of plasma inhomogeneity on the instability threshold. Then we will consider some simulations and nonlinear theory to provide estimates for how much scatter is possible.

BRILLOUIN INSTABILITY

We begin by describing the propagation of a light wave in an inhomogeneous plasma with density n(x). Maxwell's equations readily yield an equation for the evolution of the electric vector of the light:

$$\frac{\partial^2 \underline{E}}{\partial t^2} - c^2\nabla^2\underline{E} = - 4\pi\frac{\partial \underline{J}}{\partial t} \quad . \tag{IV-}$$

Here $\underline{J}$ is the plasma current density due to the response of electrons to the high frequency wave: i.e. $\underline{J} = -n(\underline{x})e\underline{u}$, where n(x) is the plasma density and $\underline{u}$ is the oscillation velocity of the electrons. Using the linearized force equation to describe the oscillation gives

$$\frac{\partial \underline{J}}{\partial t} = \frac{n(\underline{x})e^2\underline{E}}{m} \quad . \tag{IV-2}$$

Combining these two equations yields the wave equation

$$\left(\frac{\partial^2}{\partial t^2} - c^2\nabla^2 + \omega_{pe}^2(x)\right) E = 0. \qquad \text{IV-3}$$

where $\omega_{pe}^2 = 4\pi ne^2/m$.

We next specialize to one dimension, which is sufficient to treat back scatter, and decompose the density into a uniform value n_0 plus a low frequency fluctuation δn, which couples the incident light wave (E_i) to a reflected light wave (E_r). Then

$$\left(\frac{\partial^2}{\partial t^2} - c^2 \frac{\partial^2}{\partial x^2} + \omega_{pe}^2\right) E_r = -\omega_{pe}^2 \frac{\delta n}{n_0} E_i \ . \qquad \text{IV-4}$$

The physical interpretation of this equation is clear. In the presence of a low frequency density fluctuation, the oscillation of electrons in the electric vector of the incident light wave gives rise to a transverse current which generates another (reflected) light wave.

To derive an equation for the evolution of the density fluctuation, we simply use the 2-fluid description for the plasma and linearize. The low frequency component of the electron force equation gives:

$$m\frac{\partial u_e^\ell}{\partial t} = - eE^\ell - \frac{\Theta_e}{n_0}\frac{\partial \delta n}{\partial x} - \frac{e^2}{2m\omega_0^2}\frac{\partial}{\partial x}(2E_iE_r) \ ,$$

where Θ_e is the electron temperature, u_e^ℓ is the low frequency component of the velocity of the electron fluid, and ω_0 is the frequency of the incident light wave. An isothermal equation of state has been assumed, and the last term is the ponderomotive force briefly discussed in the second lecture. Neglecting electron inertia then gives

$$eE^{\ell} = -\frac{\Theta_e}{n_0}\frac{\partial \delta n}{\partial x} - \frac{e^2}{m\omega_0^2}\frac{\partial}{\partial x}\left(E_i E_r\right) \ . \qquad \text{IV 5}$$

This low frequency electric field transmits the ponderomotive force to the ions.

We next consider the continuity and force equations for the ion fluid. If we neglect ion pressure, and note that the low frequency ion density fluctuation is $\simeq \delta n$, these equations become

$$\frac{\partial}{\partial t}\delta n + n_0 \frac{\partial u_i}{\partial x} = 0 \qquad \text{IV-6}$$

$$\frac{\partial}{\partial t} u_i = \frac{Ze}{M} E^{\ell} - \nu_i u_i \ , \qquad \text{IV-7}$$

Here Z is the ion charge state and M the ion mass, and a phenomenological damping rate ν_i has been included to model Landau damping. Taking a time derivative of equation IV-6, a spatial derivative of equation IV-7, and combining yields an equation for the evolution of the density fluctuation

$$\left(\frac{\partial^2}{\partial t^2} + \nu_i \frac{\partial}{\partial t} - c_s^2 \frac{\partial^2}{\partial x^2}\right)\delta n = \frac{Z n_0 e^2}{m M \omega_0^2}\frac{\partial^2}{\partial x^2}\left(E_i E_r\right) \ , \qquad \text{IV-8}$$

where $c_s = \sqrt{Z\Theta_e/M}$ is the ion sound velocity. The physical interpretation is again clear. The incident and reflected light waves beat together to produce a fluctuation in field intensity, which drives an ion density fluctuation (ion sound wave) via the ponderomotive force.

The instability is readily obtained from the two coupled equations for E_r and δn. To derive the dispersion relation, insert $E_i = E_L \cos(k_0 x - \omega_0 t)$ and Fourier-analyze.

$$D(k,\omega)\, E_r(k,\omega) = \frac{4\pi e^2}{m} \frac{E_L}{2} \left[\delta n(k-k_0,\omega-\omega_0) + \delta n(k+k_0,\omega+\omega_0)\right] \qquad \text{IV-9}$$

$$(\omega^2 + i\omega\nu_i - k^2 c_s^2)\, \delta n(k,\omega) = \frac{Zn_0 e^2}{mM\omega_0^2} \frac{k^2 E_L}{2} \left[E_r(k-k_0,\omega-\omega_0) + E_r(k+k_0,\omega+\omega_0)\right] . \qquad \text{IV-10}$$

where $D(k,\omega) = \omega^2 - k^2 c^2 - \omega_{pe}^2$. Next choose ω to be low frequency ($\omega \ll \omega_0$), substitute equation IV-9 into equation IV-10, and neglect as off-resonant any responses with frequency $n\omega_0$ which have $|n| > 1$. This determines the dispersion relation:

$$\omega^2 + i\omega\nu_i - k^2 c_s^2 = \omega_{pi}^2 \frac{k^2 v_{os}^2}{4} \left[\frac{1}{D(\omega-\omega_0, k-k_0)} + \frac{1}{D(\omega+\omega_0, k+k_0)}\right], \qquad \text{IV-11}$$

where $v_{os} = eE_L/m\omega_0$ and ω_{pi} is the ion plasma frequency.

For back scatter $k \approx 2k_0$, and the unstable root is readily obtained. For example, for $\gamma \ll kc_s$,

$$\omega = kc_s + i\gamma ,$$

$$\gamma = \frac{1}{2\sqrt{2}} k_0 v_{os}\, \omega_{pi} / \sqrt{\omega_0 k_0 c_s} \quad . \qquad \text{IV-12}$$

If we include collisional damping of the light wave via an energy damping rate ν_L ($\nu_L = \omega_{pe}^2/\omega_o^2\nu_{ei}$, where ν_{ei} is the electron-ion collision frequency), instability requires that

$$\gamma > \sqrt{\gamma_L\gamma_i} \quad , \qquad \text{IV-13}$$

where $\gamma_L = \nu_L/2$ and $\gamma_i = \nu_i/2$. This equation defines an intensity threshold for instability:

$$\left(\frac{v_{os}}{v_e}\right)^2_{Th} \approx 2\,\frac{\nu_{ei}}{\omega_o}\,\frac{\nu_i}{k_oc_s} \quad .$$

In practice, the threshold intensity is usually determined by gradients in the plasma density and expansion velocity rather than by collisions. Plasma inhomogeneity limits the region over which three waves can resonantly interact. and propagation of wave energy out of this region introduces an effective dissipation which must be overcome. Noting that the wave numbers are now a function of position, let us define $K = k_1(z) - k_2(z) - k_3(z)$. At some point. $K \approx 0$ (i.e., the waves are resonantly coupled), but away from this point a mismatch develops. The resonant coupling is spoiled when a significant phase shift develops. Hence we can estimate the size ℓ_{int} of the interaction region by the condition $\int_0^{\ell_{int}} K dz \sim 1/2$ Taylor expanding about the matching point ($K = K(0) + K^1 z$) then gives

$$\ell_{int} \sim \frac{1}{\sqrt{K'}} \quad . \qquad \text{IV-14}$$

Propagation of wave energy out of this interaction region introduces an effective damping rate of approximately v_{gi}/ℓ_{int}, where v_{gi} is the group velocity of the ith wave. Inserting these damping rates into equation IV-13 then gives the Rosenbluth condition[31] for amplification in an inhomogeneous plasma:

$$\frac{\gamma^2}{|K' v_{g1} v_{g2}|} > 1 \quad . \qquad \text{IV-15}$$

where 1 and 2 refer to the growing waves. If we apply this equation to Brillouin back scatter in a plasma with a density gradient length L, $K' \sim \omega_{pe}^2/c\omega_o L$, and the threshold condition becomes

$$\left(\frac{v_{os}}{v_e}\right)^2_{Th} \sim \frac{8}{k_o L} \quad . \qquad \text{IV-16}$$

NONLINEAR EVOLUTION OF BRILLOUIN BACK SCATTER

What controls the level of the Brillouin scatter when the threshold intensity is far exceeded? To gain insight into the nonlinear behavior of this instability, let us first consider some computer simulations of Brillouin backscatter[32,33] and then briefly discuss some nonlinear estimates.

The simulations[32] we will *discuss here are carried out using a* 1.5 dimensional particle code (two velocities, one spatial dimension) which allows for electromagnetic waves and relativistic particle dynamics. To focus on back scatter, intense laser light is propagated through a slab of totally underdense plasma with an initial density profile rising from zero to 0.7 n_{cr} in 10 λ_0. The initial electron temperature is 1 keV, the initial ion temperature is 0.2 keV, and the ion-electron mass ratio is 300. A region of vacuum is included at both boundaries, and electromagnetic waves either reflected or transmitted are allowed to freely pass out of the system.

Fig. 13 shows the evolution of the reflectivity computed *in a sample simulation. In this simulation*, the incident laser light has an intensity such that $eE_L/m\omega_0 c \simeq 0.1$ where E_L is the free-space value of the electric vector of the light. This corresponds to an intensity of $\simeq 10^{16}$ W/cm^2 for 1.06 μ light, which is far above the threshold intensity. Note that the reflectivity rapidly increases as the ion waves grow. It finally saturates at a value of $\simeq$ 50% as the ion wave amplitude becomes limited by ion trapping.

The variation of the reflectivity with incident intensity is shown in Fig. 14, which is a plot of the fraction of the incident light energy which is Brillouin back scattered as a function of $(v_{os}/v_e)^2$. This reflection is averaged over a time much greater than the time for *instability growth and saturation, but is short-term in* the sense that gross changes in either the density profile or background plasma conditions can occur on a longer time scale. A significant reflectivity onsets when the intensity is about 3-4 times the intensity threshold due to the density gradient, which is estimated in equation IV-16. The reflectivity subsequently increases with intensity up to values of 30-50%, even for this rather small plasma.

Insight into the size of the scatter can be gained by a very simple nonlinear model. Assuming that the instability is well above the thresholds set by gradients, let us consider a slab of uniform underdense plasma with density n_p and length L. Further we will assume that the ion wave associated with Brillouin back scatter has been driven to a value δn limited by ion trapping as typically shown by the simulations. If we separate out the fast time and space dependences, equation IV-4 and the analogous equation for E_i give

$$\frac{\partial E_r}{\partial x} = \kappa \frac{\delta n}{n_p} E_i \qquad \text{IV 17}$$
$$\frac{\partial E_i}{\partial x} = -\kappa \frac{\delta n}{n_p} E_r$$

where E_r and E_i are the slowly varying amplitudes and

$$\kappa = \frac{\omega_0}{2}\frac{\omega_{pe}^2}{\omega_0^2} \Big/ \left[c_0 \left(1 - \frac{\omega_{pe}^2}{\omega_0^2}\right)^{1/2} \right] .$$

These coupled equations are readily integrated to determine the reflectivity, r. Assuming that $E_r(L) \ll E_i(0) = E_L$, we then find

$$r = \tanh^2 \kappa L , \qquad \text{IV 18}$$

where [illegible] $\frac{\delta n}{n_p} L$.

To estimate the value of the density fluctuation in the trapping limit, we appeal to an argument similar to that discussed in the second lecture. Consider an ion wave with potential ϕ and treat the ions as a waterbag distribution. Then the condition that the fastest ion be brought to rest in the wave frame (i.e., be nonlinearly brought into resonance) is

$$-e\phi + \frac{M}{2}(c_s - \sqrt{3}\,v_i)^2 = 0 \quad ,$$

where M is the ion mass and c_s is the ion sound velocity. The corresponding value of the density fluctuation, $\frac{\delta n}{n_p} = \frac{e\phi}{\theta_e}$, is

$$\frac{\delta n}{n_p} = \frac{1}{2}\left(\sqrt{1 + \frac{3\theta_i}{\theta_e}} - \sqrt{\frac{3\theta_i}{\theta_e}}\right)^2 \quad . \qquad \text{IV-19}$$

As an example, let us consider $\theta_i/\theta_e = 0.2$, $\omega_{pe}^2/\omega_o^2 = 0.35$ (its average value in the sample simulation), and $L = 10\lambda_o$. Then equation IV-19 predicts $\delta n/n_p \simeq 0.12$. And equation IV-18 predicts $\sim$ 45%, comparable to the reflectivities observed at the higher intensities.

Although these calculations provide a rough estimate of the size of the short-term scatter, they can clearly overestimate the net scatter in experiments. There are several different long-term effects which lower the scatter as emphasized by both simulations and theory. First, if the light pressure is much greater than the plasma pressure in the underdense region, the momentum deposition due to the reflecting light can gradually push the underdense plasma out of the way.[34] Secondly, even if the light pressure is less than or comparable to the plasma pressure, there can be a very significant long-term heating of the ions by the ion waves. As the effective ion temperature increases, the ion wave amplitude decreases, lowering the reflectivity. Recent calculations[35] focusing on this long-term self-consistent ion heating (tail formation) indicate that hundreds of wavelengths of underdense plasma are then needed to provide a reflectivity of ~ 50%.

Finally, it is not yet known how multi-dimensional effects modify these results. Back scatter has the largest growth rate, but the Brillouin instability can of course scatter light over a broad range of angles. Indeed, in an inhomogeneous plasma, side scatter has a lower threshold intensity than does back scatter, since the side scattered light wave spends a longer time in the interaction region. There are also other multi-dimensional effects which must be considered. For example, a perturbation in the intensity profile of the incident light beam creates a depression in plasma density via the ponderomotive force. This density depression refracts the light inward, increasing the intensity perturbation. The result is the so-called filamentation instability[36], which can lead to a break up of the incident light beam into intense filaments. This instability has a smaller growth rate than the Brillouin instability unless the ion and electron temperatures are comparable, but little is known about the competition of these effects in the nonlinear state.

LECTURE FIVE: COMPARISON OF CALCULATIONS WITH EXPERIMENTS

INTRODUCTION

In the previous lectures, we discussed a number of different processes which play a role in the coupling of intense laser light with plasmas. These processes were chosen to illustrate general features of the light-plasma coupling. For example, in the second and third lectures, we described enhanced absorption of laser light via its coupling into plasma waves near the critical density. Important features of this coupling were nonlinear profile steepening and the generation of high energy electrons. In the fourth lecture, we described enhanced reflection of laser light via its stimulated scattering by ion acoustic waves in the lower than critical density plasma. The calculations indicated that a sizeable reflectivity was possible in large underdense plasmas. In this final lecture, let us consider some of the experimental evidence for these various plasma processes.

From a theoretical viewpoint, it is clearly appropriate to divide laser plasma experiments into two rather broad categories depending upon the size of the underdense plasma. If the characteristic size L of the underdense plasma is small ($L/\lambda_0 \lesssim \mathcal{O}(10)$, where λ_0 is the free space wavelength of the light), then it has little effect on the incident light, and one is primarily investigating how light is absorbed near the critical density surface. On the other hand, if there is an extensive region of underdense plasma $[L/\lambda_0 \gtrsim O(100)]$, theory indicates that effects such as Brillouin scatter, filamentation, and inverse bremsstrahlung can play a sizeable role.

We can estimate the size of the underdense plasma in laser-irradiated targets as the minimum of $c^* \tau$ or R, where c^* is a typical plasma expansion velocity, τ is the pulse length of the laser light, and R is the focal spot radius. To give some feeling for the members, $L/\lambda_0 \sim [3 \times 10^2 \tau (ns), R(\mu)]_{min}/\lambda_0(\mu)$, where an expansion velocity of 3×10^7 cm/sec has been taken, τ is measured in ns, and R and λ_0 are measured in μ. Hence experiments with 1.06 μ light and pulse lenths of $\lesssim$ 30 ps have rather small underdense plasmas, whereas experiments with pulse lengths $\gtrsim$ 1ns have large underdense plasmas. Note also the scaling as $1/\lambda_0$. With this distinction in mind, we will first examine some short-pulse-length experiments (with small underdense plasmas) and then briefly consider some longer pulse-length ones.

DENSITY PROFILE STEEPENING

As we discussed in the third lecture, calculations predict a pronounced steepening of the density profile near the critical density. This steepening is very important because the scale length near the critical density affects the mix of absorption processes and the heated electron temperatures. This profile steepening has been confirmed by interferometric measurements of the density of a laser-heated plasma. In the experiment[37] a 41-μ diameter glass microballoon was irradiated with a 30 ps, 1.06 μ laser pulse at an intensity of 3×10^{14} W/cm^2. An interferomgram was taken and Abel-inverted to determine the axial electron density profile plotted in Fig. 15. In both experiment and the simulations discussed in the third lecture, the profile is steepened to an upper density n_u that is roughly determined by pressure balance:

$$n_u \quad n_{cr} \left[1 + (v_{os}/v_e)^2 \right] ,$$

where v_{os} is the oscillation velocity of an electron in the laser light field, v_e is the electron thermal velocity, and n_{cr} is the critical density. The profile is steepened down to a lower density that is determined by how the light pressure and localized heating dams the plasma flow. This lower density typically appears to be somewhat less in experiments than in the particle simulations, perhaps because of energy-transport inhibition.

Calculations with a focused light beam[38] show an additional effect: cratering of the critical density surface. Physically, the density surface is preferentially pushed in where the light intensity is greatest. This effect has also been observed in experiments. Fig. 16 shows an Abel inverted density contour measured in an experiment[37] in which a disk target was irradiated with 1.06 μ light with an intensity of $\simeq 3 \times 10^{14}$ W/cm^2. The density cavity has a transverse scale approximately equal to that of the incident light beam. A smaller scale rippling of the critical density surface has also been inferred in experiments using higher intensity light. These ripples are probably due to hot spots in the incident light beam and/or to a critical surface instability found in computer simulations.[39]

ABSORPTION OF INTENSE, SHORT PULSE-LENGTH LIGHT

Calculations have also predicted many important features of the absorption in experiments with short pulse length, high intensity laser light. In such experiments, the underdense plasma has both a high temperature and a small spatial extent. Because collisional absorption varies as $\theta_e^{-3/2}$ (θ_e is the electron temperature) and as the scale length of the plasma, it is weak in these experiments. However, as discussed in the third lecture, computer simulations showed that there would still be a sizeable absorption due principally to resonance absorption with a small additional absorption due to nonlinearly-generated ion fluctuations. These early simulation results assumed plane waves incident onto a plasma slab. In practice, a focussed light beam (say, with hot spots) both craters and ripples the critical density surface as discussed in the previous section. These surface ripples average the absorption over angle as well as change part of the p-polarized light into s-polarized light and vice versa. A simple theory[40] was used to extend the ideal simulation results to crudely include this additional critical surface rippling. The result for the absorption as a function of polarization and angle of incidence is shown by the black line in Fig. 17.

The absorption was measured in detail in recent experiments.[41,42] In these experiments,[41], plastic disks were irradiated with about 30 ps pulses of 1.06 μ light with an intensity of 10^{15} - 10^{16} W/cm^2. The measured absorption, denoted by the circles in Fig. 17, was both polarization-dependent and broad in angle. The absorption of p-polarized light peaked at approximately the predicted angle, and the absorption of s-polarized light monotonically decreased with angle of incidence. The magnitude of the absorption was also in reasonable agreement. The principal discrepancy is an additional 10-15% absorption, rather independent of angle of incidence and polarization. This additional absorption may be due to ion turbulence generated by heat-flow instabilities, self-generated magnetic fields, or the $2\omega_{pe}$ instability.

HEATED ELECTRON TEMPERATURES

A very important question is the magnitude of the heated-matter energy produced when laser light is absorbed. This light primarily heats electrons, since their motion in the oscillating fields is much larger than that of the massive ions. As discussed in the second and third lectures, absorption via plasma waves does not in general lead to a simple temperature electron distribution. Physically this is because plasma waves tend to preferentially heat the faster (more nearly resonant) electrons. The simulations of resonance absorption discussed in the third lecture predict that a two-temperature distribution will result. The lower temperature is that typical of electrons streaming into the absorption region and is determined by how the heat transports to higher density. The hot temperature is that characteristic of the electrons heated by resonance absorption, which the simulations predict will have a quasi-Maxiwillian distribution.[43]

The existence of a two-temperature electron distribution is supported by measurements of the x-ray spectrum in many different experiments using short-pulse-length laser light. As an example, Fig. 18 shows the x-ray spectrum observed in an experiment[44] in which a plastic disk was irradiated with a 80 ps pulse of 1.06 μ light at a peak intensity of ≈ 2 x 10^{15} /cm^2. The low energy x-rays indicate a temperature of ≈ 700 ev, and the high energy x-rays a temperature of ≈ 8 keV.

Fig. 19 shows the heated electron temperature inferred from the high energy x-rays over a wide intensity regime. The various symbols with error bars represent experimental data from a series of experiments[45] in which disks or microballoons were irradiated with 1.06 μ light with pulse lengths in the range of about 50-200 ps. The open x's are values of the resonantly-heated electron temperature calculated in a series of two dimensional simulations[43] of resonance absorption. Both the magnitude and intensity scaling of the heated electron temperatures are in reasonable agreement, especially in view of the fact that the simulations are quite ideal and do not include the space-and time-averaging inherent in the experiments. Experiments using laser light with other wavelengths have given quite similiar results. One simply has to scale the intensity as $I\lambda_0^2$ (where λ_0 is the free-space wavelength of the light), as theoretically expected.[46]

We expect that the high energy x-ray spectrum will not in general indicate only a single hot electron temperature. Resonance absorption is not the only process heating the plasma. For example the Raman and $2\omega_{pe}$ instabilities each produce hot electrons in the lower than critical density plasma. Such effects will probably be especially noticeable in longer pulse-length experiments. In fact, recent experiments[47] using 1ns pulses of 1.06 μ light do indicate the presence of hot electrons with several different temperatures.

BRILLOUIN SCATTER

We have been discussing short-pulse-length experiments; that is, experiments characterized by a small region of plasma with density less than n_{cr}. Such experiments have been typical of the exploding-pusher target experiments carried out in the past--early laser fusion experiments with violent nonadiabatic compression of deuterium-tritium gas to high temperature but to a density of only about 0.1 g/cm^3. Prescriptions for the calculated absorption and hot electron temperature were incorporated into a target design code, which did reasonably well in tracking these implosion experiments.[48]

Laser-plasma coupling is more difficult to compute in long-pulse-length experiments, however, because the underdense plasma is then much larger. In large regions of underdense plasma, effects such as collisional absorption, Brillouin and Raman scattering, and filamentation can all play a much more important role in the laser plasma coupling. In general, the magnitude of these effects and their competition is poorly understood, both theoretically and experimentally.

Some progress has been made in beginning to understand the important role of Brillouin scatter in long-pulse-length experiments. Both simulations and a simple theoretical model were used to predict sizeable Brillouin scatter in experiments[49] with large regions of underdense plasma. As shown in Fig. 20, this backscatter was predicted to be on the order of 50% when the characteristic size of the underdense plasma becomes about 100 free-space laser light wavelengths. The line is the prediction of a simple theoretical model for Brillouin backscatter, which takes into account the self-consistent ion heating that accompanies the instability. The squares denote simulation results using a hybrid code with fluid electrons and particle ions.

Experiments[49] in which plastic disks were irradiated with 1.06 μ light with pulse lengths of 200 to 400 ps and focused intensities of about 3 x 10^{15} to 3 x 10^{16} W/cm^2 support these predictions. As shown in Fig. 21, the absorption was found to be reduced by a factor of about two in these experiments as compared with that observed in the analogous short-pulse-length experiments. Measurements of the frequency spectra of the reflected light showed frequency shifts consistent with Brillouin scatter. Subsequent longer pulse-length (1ns) experiments[50] using high-Z targets have also indicated sizeable Brillouin scatter.

A larger underdense plasma can also be created by use of a prepulse. As shown in Fig. 22, the addition of a prepulse about 2 ns prior to a 75 ps main pulse was found[51] to increase the backscatter of the main pulse which was normally incident onto a CH slab. As the prepulse energy was increased, the fraction of the main pulse which was back-reflected increased from ≃ 15% to ≃ 40% and the net absorption decreased from ≃ 50% to ≃ 20%. For a fixed ratio of prepulse energy to main pulse energy, the back-scattered light increased with the intensity of the main pulse and was rather insensitive to the angle at which the targets were tilted, as shown in Fig. 23. In addition, it was found that the light rays retraced their path. All these features are as expected if the light reflection is due to the Brillouin instability in the underdense plasma.

OTHER PLASMA PROCESSES

Finally, there is also experimental evidence for many other plasma processes in laser-produced plasmas. These processes include:

1. Brillouin side scatter as inferred from a substantial asymmetry[52] of the scattered light with respect to its plane of polarization;
2. filamentation as inferred from hot spots[52] in x-ray microscope pictures of the heated plasma or from enhanced intensity structure in the reflected and transmitted beam;
3. instabilities near one-fourth the critical density as deduced from one-half and three-halves harmonic emission;[53]
4. self-generated magnetic fields, which have been measured[54] at values of several mega-gauss;
5. and parametrically-generated ion turbulence near the critical density as inferred from frequency shifts in the second harmonic emission.[55] A more detailed discussion of these many different effects is beyond the scope of this lecture.

In summary, plasma processes play a significant role in the coupling of intense laser light to targets. Calculations have predicted many important features of laser plasma experiments. In turn, the experimental feedback has been very important. Although encouraging progress has been made, the understanding is weak in many crucial areas. For example, there is a great deal to learn about the competition of inverse bremsstrahlung, Brillouin back and side scatter, and filamentation in long-pulse-length experiments. In addition, we need to develop an improved understanding of electron transport and the various mechanisms which can inhibit this transport.

ACKNOWLEDGMENTS

I am very grateful for collaboration and discussion over the years with many colleagues, especially J. Dawson, J. Nuckolls, K. Estabrook, E. Valeo, J. Thomson, B. Langdon, B. Lasinski, R. Faehl, C. Max, C. Randall, W. Mead, M. Rosen, H. Shay, R. Haas, D. Phillion, and V. Rupert.

REFERENCES

1. This lecture is primarily based on the article: W. L. Kruer, Nuclear Technology 27, 216 (1975).
2. O. Buneman, Phys. Rev. 115, 503 (1959).
3. J. M. Dawson Phys. Fluids 5, 445 (1962).
4. R. L. Morse and C. W. Nielsen, Phys. Rev. Letters 23, 1087 (1969).
5. C. K. Birdsall and D. Fuss, J Comp Physics 3 494 (1969).
6. J. P. Boris and K. V. Roberts, J. Comp. Physics 4, 552 (1969).
7. W. L. Kruer, J M Dawson, and B. Rosen, J Comp Physics 13, 114 (1973).
8. Methods in Computational Physics, Vol. 9. Edited by B. Alder, S Fernback and M. Rotenburt (Academic Press, N.Y., 1970).
9. Proceedings of the Fourth Conference on Numerical Simulation of Plasmas, Edited by J. P. Boris and R. Shanny (Office of Naval Research, Wash., D.C. 1970).
10. A. B. Langdon, J. Comp. Physics 6, 247 (1970).
11. J. Denavit and W. L. Kruer, Phys. Fluids 14, 1782 (1971).
12. W. L. Kruer, J. M. Dawson, and R. N. Sudan, Phys. Rev. Letters 23, 838 (1969).
13. C. B. Wharton, J. H. Malmberg and T. M. O'Neil, Phys. Fluids 11, 1761 (1968).
14. A. B. Langdon and B. F. Lasinski, in Methods in Computational Physics, Edited by J. Killen, B. Alder, S. Fernbach, and M. Rotenberg, Vol. 16 p. 327 (Academic, New York, 1976).
15. T. W. Johnston and J. M. Dawson, Phys. Fluids 16, 722 (1973).

16. K. Nishikawa, J. Phys. Soc. Japan 24, 916, 1152 (1968);
V. P. Silin, Sov. Phys. JETP 30, 105 (1970).

17. W. L. Kruer and J. M. Dawson, Phys. Fluids 15, 446 (1972).

18. H. Dreicer, R. Ellis, and J. Ingraham, Phys. Rev. Letters 31, 426 (1973).

19. T. P. Coffey, Phys. Fluids 14, 1402 (1971).

20. For a more extensive review, see W. L. Kruer, in *Advances in Plasma Physics*, edited by A. Simon and W. Thompson (Wiley, New York, 1976), Vol. 6, p. 237.

W. L. Kruer, Lawrence Livermore Laboratory UCRL-81396 (1978

22. V. L. Ginzburg, *The Propagation of Electromagnetic Waves in Plasmas* (Pergamon, NY 1965), p. 260.

23. J. P. Freidberg, R. W. Mitchell, R. L. Morse and L. F. Rudsinski, Phys. Rev. Letters 28, 795 (1972).

24. K. G. Estabrook, E. J. Valeo, and W. L. Kruer, Phys. Fluids 18, 1151 (1975).

25. D. W. Forslund, J. M. Kindel, K. Lee, E. L. Lindman and R. L. Morse, Phys. Rev. A11, 679 (1975).

26. J. S. DeGroot and J. Tull, Phys. Fluids 18, 672 (1975).

27. P. Koch and J. Albritton, Phys. Rev. Letters 32, 1420 (1974.

28. W. L. Kruer, Phys. Fluids 22, 1111 (1979).

29. D. F. Dubois and M. V. Goldman, Phys. Rev. Letters 14, 544 (1965).

30. C. S. Liu, in *Advances in Plasma Physics*, edited by A. Simon and W. Thompson (Wiley, New York, 1976), Vol. 6.

31. M. N. Rosenbluth, Phys. Rev. Letters 28, 565 (1972).

32. W. L. Kruer, K. G. Estabrook, and K. Sinz, Nuclear Fusion 13, 952 (1973).

33. D. W. Forslund, J. M. Kindel and E. Lindman, Phys. Rev. Letters 30 739 (1973); also Phys. Fluids 18, 1017 (1975).

34. W. L. Kruer, E. J. Valeo, and K. G. Estabrook Phys. Rev. Letters 35, 1076 (1975).

35. D. W. Phillion, W. L. Kruer and V. C. Rupert, Phys. Rev. Letters 39, 1529 (1977).

36. P. K. Kaw, G. Schmidt, and T. Wilcox, Phys. Fluids 16, 1522 (1973).

37. D. T. Attwood, D. W. Sweeney, J. M. Auerback, and P. H. Y. Lee, Phys. Rev. Letters 40, 184 (1978), see also R Fedosejevs et al., Phys. Rev. Letters 39, 932 (1977).

38. C. Randall and J. DeGroot, Phys. Rev. Letters 42, 179 (1979).

39. K. G. Estabrook, Phys. Fluids 19, 1733 (1976).

40 J. J. Thomson, W. L. Kruer, A. B. Langdon, C. E. Max, and W. C. Mead, Phys. Fluids 21, 707 (1978).

41. K. R. Manes, V C. Rupert, J. M. Auerbach, P. Lee, and J. E. Swain, Phys. Rev. Letters 39, 281 (1977).

42 R. P. Godwin, P. Sachsenmaier, and R. Sigel, Phys. Rev. Letters 39, 1198 (1977); J. S. Pearlman and M. K. Matzen, Phys. Rev. Letters 39, 140 (1977); J. E. Balmer and T. P. Donaldson, Phys. Rev. Letters 39, 1084 (1977).

43. K. G. Estabrook and W. L. Kruer, Phys. Rev. Letters 40, 42 (1978).

44. R. Haas et al., Phys. Fluids 20, 322 (1977).

45. K. R. Manes et al., J. Opt. Soc. Am. 67, 717 (1977).

46. D. W. Forslund, J. M. Kindel and K. Lee, Phys. Rev. Letters 39, 284 (1977).

47. W. Slivinsky (private commumications).

48. M. D. Rosen and J. H. Nuckolls, Phys. Fluids 22, 1393 (1979).

49. D. W. Phillion, W. L. Kruer, and V. C. Rupert, Phys. Rev. Letters 39, 1529 (1977).

50. M. D. Rosen et al; Phys. Fluids (in press).

51. B. H. Ripin et al., Phys. Rev. Letters 39, 611 (1977).

52. H. D. Shay et al., Phys. Fluids 21, 1634 (1978).

53. S. Jackel, J. Albritton, and E. Goldman, Phys. Rev. Letters 35, 514 (1975); D. W. Phillion (private communication).

54. B. H. Ripin et al., Phys. Rev. Letters 34, 138 (1975).

55. N. G. Basov et al., in *Plasma Physics :Nonlinear Theory and Experiments*, edited by H. Wilhelmsson. (Plenum, New York, 1977), p.47

FIGURE CAPTIONS

Fig. 1. A schematic of the basic cycle of a plasma simulation code using particles.

Fig. 2. The computed evolution[11] of the wave energy in a large amplitude plasma wave (upper curve) and in its lower sideband (lower curve). The open (solid) symbols are results from the Vlasov equation (particle code).

Fig. 3. The experimentally measured evolution[13] of the energy in a large plasma waves and in its lower sideband.

Fig. 4. A schematic of a 2 D simulation of plasma heating by laser light using an electromagnetic, relativistic particle code.

Fig. 5. A schematic illustrating the feedback mechanism leading to instability.

Fig. 6. The computed evolution[17] of a) the plasma wave energy and b) the kinetic energy of a plasma driven by a electric field oscillating near ω_{pe}.

Fig. 7. A typical heated electron velocity distribution predicted[17] by the particle code.

Fig. 8. A heated electron velocity distribution measured in an experiment[18] on anomalous plasma heating by microwaves.

Fig. 9. A sketch illustrating a light ray obliquely incident onto an inhomogeneous plasma slab.

Fig. 10 A plot of the function $\phi(\tau)$, which characterizes the efficiency of resonance absorption. The dashed line is the simple estimate derived in the text. The solid line is from reference 22.

Fig. 11. The ion density profile from the sample simulation[24] at three different times: a) the initial profile, b) the profile after the resonant field has grown, and c) the asymptotic profile which shows a characteristic step-plateau feature.

Fig. 12. The fractional absorption after profile steepening vs angle of incidence. as computed in a series of simulations[24] with the same initial plasma conditions as the sample simulation discussed in the text.

Fig. 13. The evolution of the back reflection computed in the sample simulation discussed in the text.

Fig. 14. The scaling of the short-term back reflection with $(v_{os}/v_e)^2$, as computed in a series of simulations[32] with the same initial plasma conditions as the sample simulation discussed in the text. Here $v_{os} = eE_L/m\omega_0$, and v_e is the initial electron thermal velocity.

Fig. 15. A measured density profile[37] in a laser-irradiated target. A 1.06 μ laser pulse with an intensity of about 5×10^{14} W/cm^2 was incident onto a glass microsphere. The profile was measured by interferometry using a frequency doubled light pulse

Fig. 16. An axial density profile measured by interferometry.[37] In this experiment, a 1.06 μ laser pulse with an intensity of about 3 x 10^{14} W/cm^2 was incident onto a flat disc.

Fig. 17. Absorption as a function of angle of incidence and polarization for (a) p-polarization and (b) s polarization. Black lines are obtained by modifying the simulation results discussed in the third lecture to include an additional rippling of the critical density surface due to inhomogeneities in the incident light beam. Circles denote the absorption that was measured in a series of experiments in which plastic disks were irradiated. The 1.06-μm light was focused with an f/10 lens to an incident intensity in the range of 10^{15} to 10^{16} W/cm^2.

Fig. 18. The x-ray spectrum measured in an experiment[44] in which a plastic disc was irradiated by a 50 ps pulse of 1.06 μ light with an intensity of about 2 x 10^{15} W/cm^2.

Fig. 19. The heated electron temperature as a function of intensity. The various symbols with error bars represent the values inferred from the high energy x-rays in experiments[45] in which disks or microballoons were irradiated with 1.06-μm light. The triangles are values calculated in a series of two-dimensional simulations using plane waves incident onto a plasma slab.

Fig. 20. The fraction of the incident light that is Brillouin backscattered as a function of the size of a uniform underdense plasma. The lines are results from a one-dimensional theoretical model in which ion heating by the driven ion waves provides the stabilization. The squares denote simulation results using a one-dimensional code. The initial electron temperature was 2 keV; the incident light intensity was 2 x 10^{15} W/cm^2.

Fig. 21. The absorption as a function of pulse length and focal spot size measured in an experiment[49] in which plastic disks were irradiated with 1.06-μm light. The experiments with longer pulse lengths and, hence, larger regions of underdense plasma exhibited less absorption, consistent with the presence of Brillouin scatter.

Fig. 22. The fraction of the main pulse energy which was back reflected versus the prepulse level.[51] The prepulse was introduced 2 ns prior to the main 75 ps (FWHM) pulse, which has a focused intensity of ≃ 5-10 x 10^{15} W/cm^2.

Fig. 23. Back reflection of the main laser pulse[51] versus a) target angle Θ and b) the incident energy or intensity. ((o)Θ = 0°, (●) Θ = 45°). The ratio of the prepulse energy to the main pulse energy was 0.2.

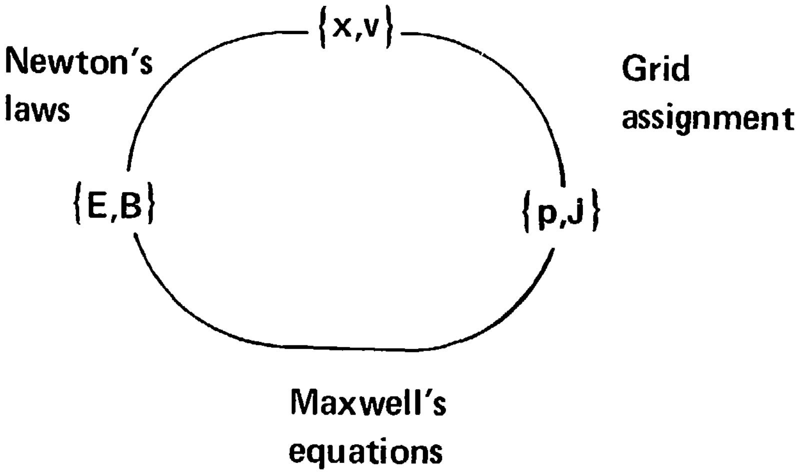

Fig. 1

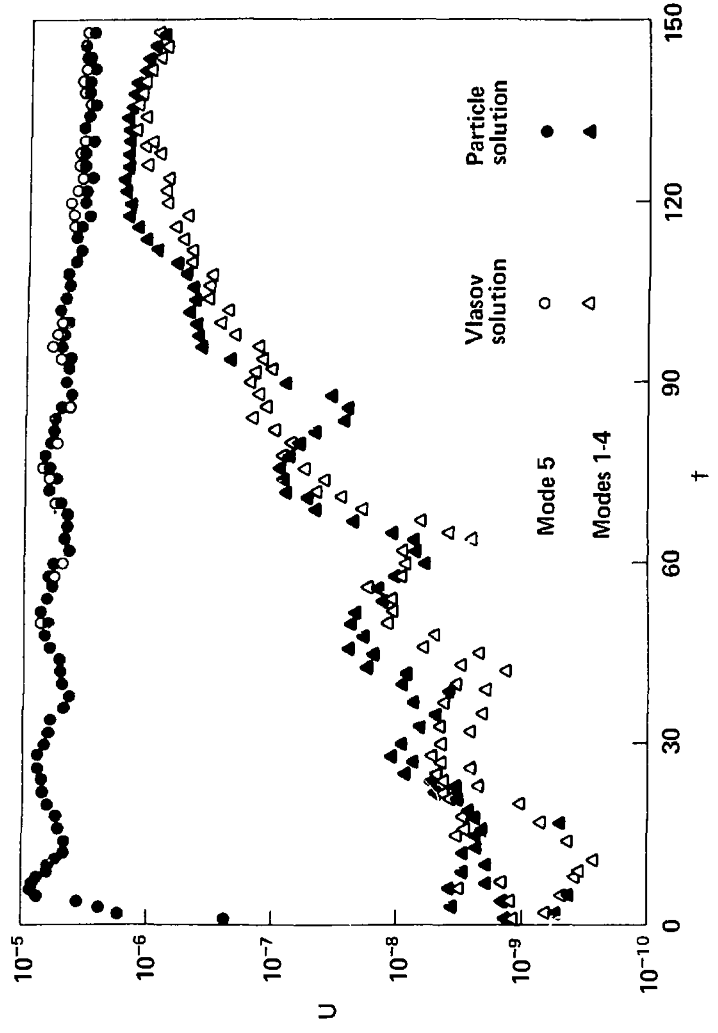
U
10^{-5}
10^{-6}
10^{-7}
10^{-8}
10^{-9}
10^{-10}
t
0
30
60
90
120
150
Vlasov solution
Particle solution
Mode 5 ○ ●
Modes 1-4 △ ▲

Fig. 2

Fig. 3

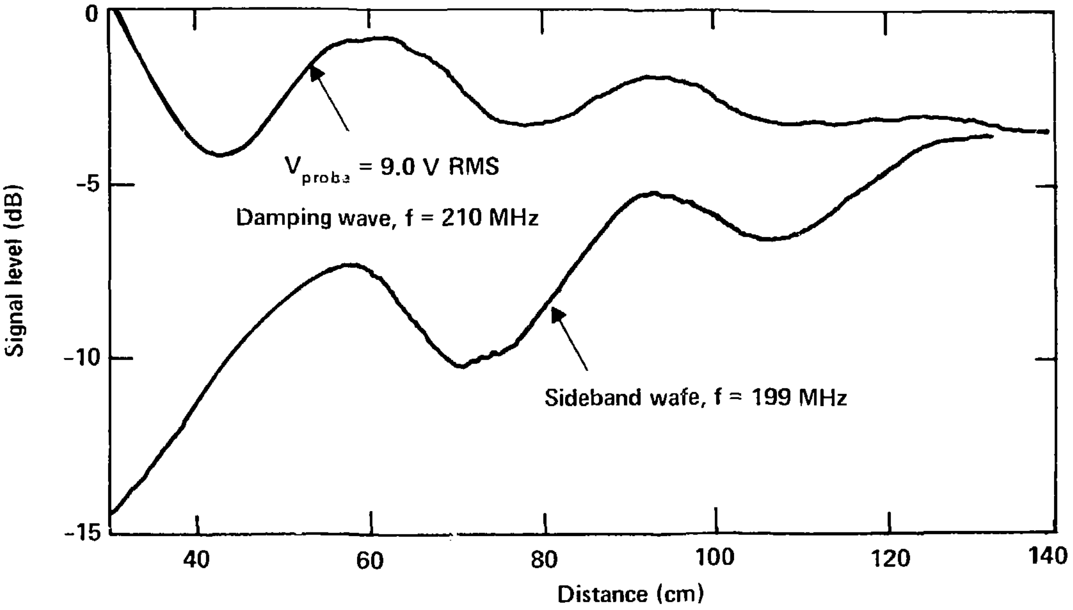
0
-5
-10
-15
40
60
80
100
120
140
Distance (cm)
Signal level (dB)
Vprobe = 9.0 V RMS
Damping wave, f = 210 MHz
Sideband wafe, f = 199 MHz

Fig. 4

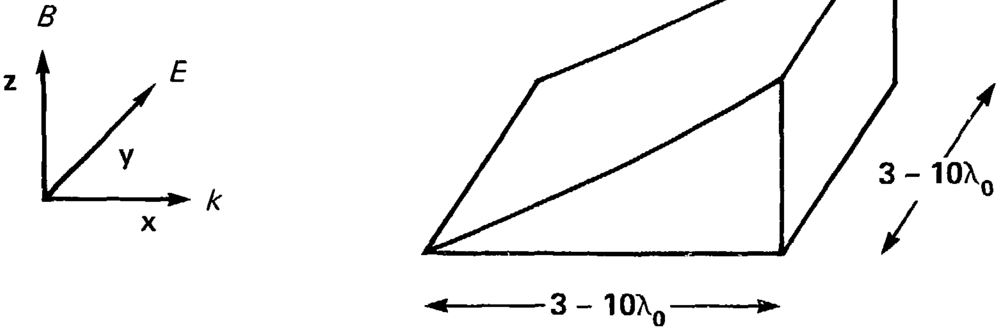

X, Y, V_x, V_y Allow variations in two directions (x and y).

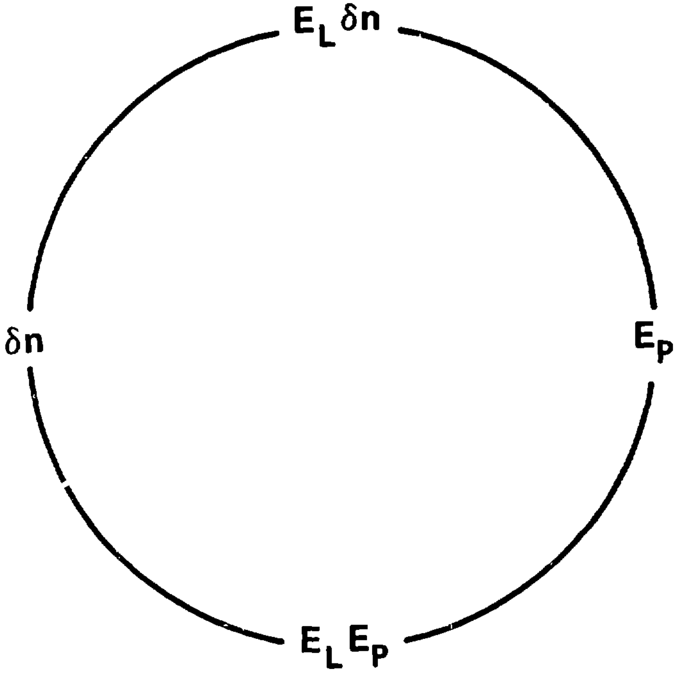

Fig. 5

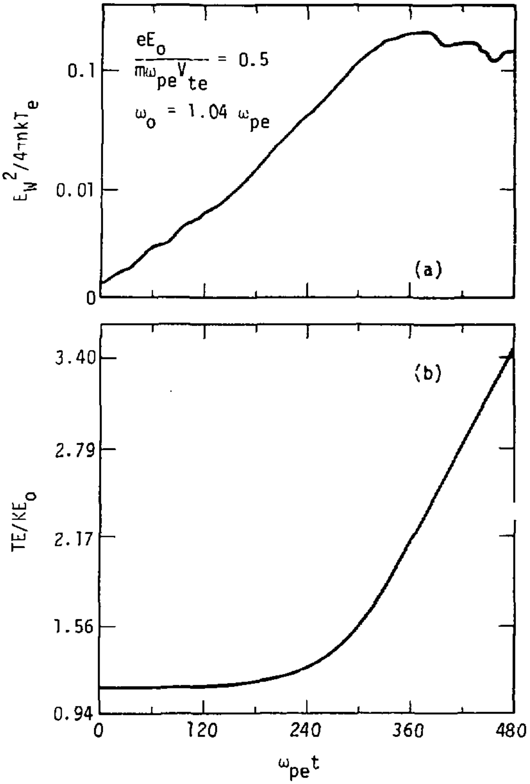$\frac{eE_o}{m\omega_{pe}V_{te}} = 0.5$
$\omega_o = 1.04\ \omega_{pe}$
$E_W^2/4\pi nkT_e$
0.1
0.01
0
(a)
(b)
TE/KE$_o$
3.40
2.79
2.17
1.56
0.94
0
120
240
360
480
$\omega_{pe}t$

Fig. 6

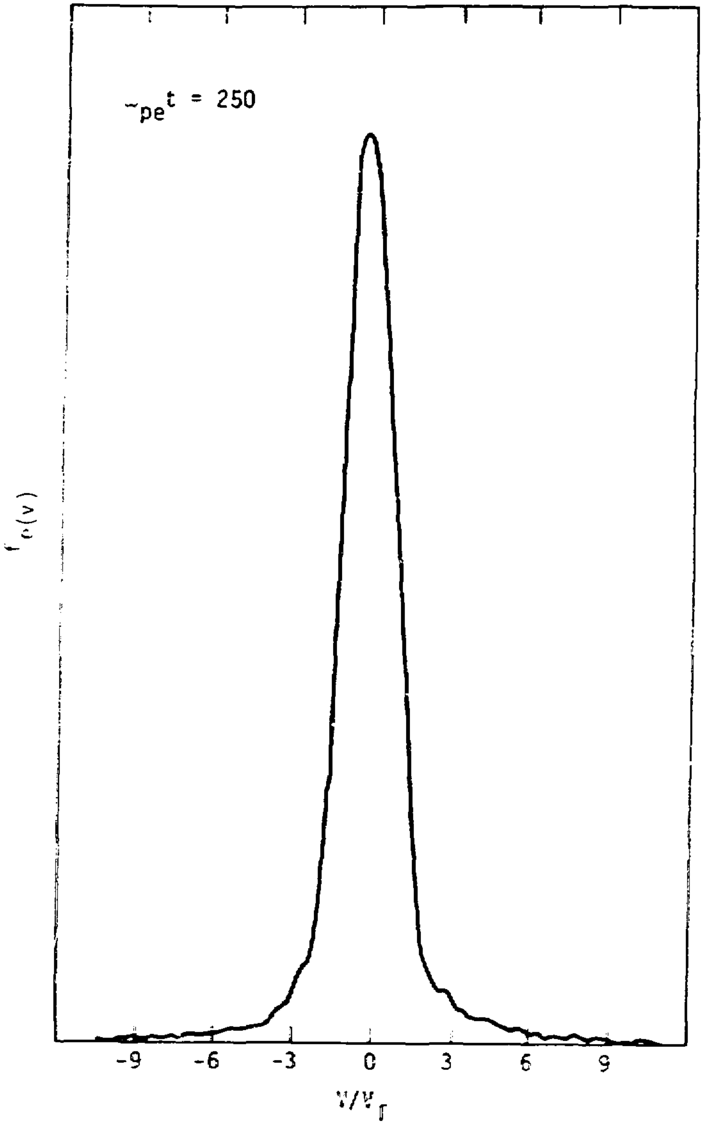

Fig. 7

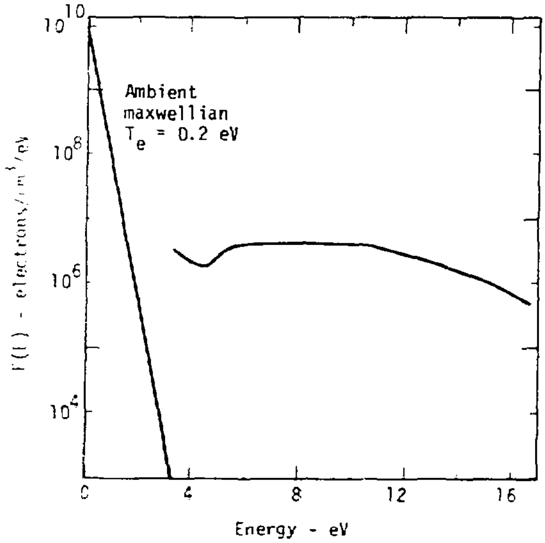

10^{10}
10^{8}
10^{6}
10^{4}
F(E) - electrons/cm^3/eV
Ambient
maxwellian
T_e = 0.2 eV
0
4
8
12
16
Energy - eV

Fig. 8

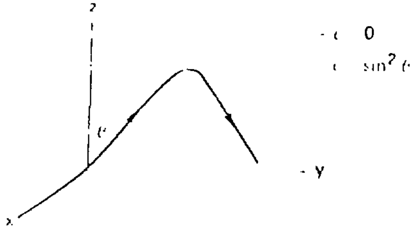
z
θ
0
sin² θ
y
x

Fig. 9

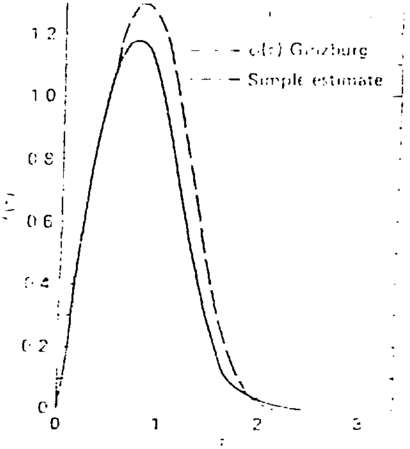
1.2
1.0
0.8
0.6
0.4
0.2
0
0
1
2
3
ε(z) Ginzburg
Simple estimate

Fig. 10

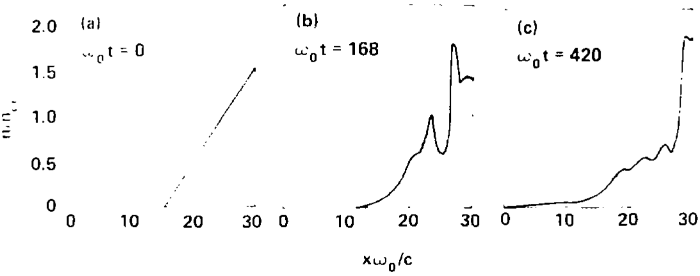
2.0
1.5
1.0
0.5
0
n/n_c
(a)
$\omega_0 t = 0$
(b)
$\omega_0 t = 168$
(c)
$\omega_0 t = 420$
0
10
20
30
0
10
20
30
0
10
20
30
$x\omega_0/c$

Fig. 11

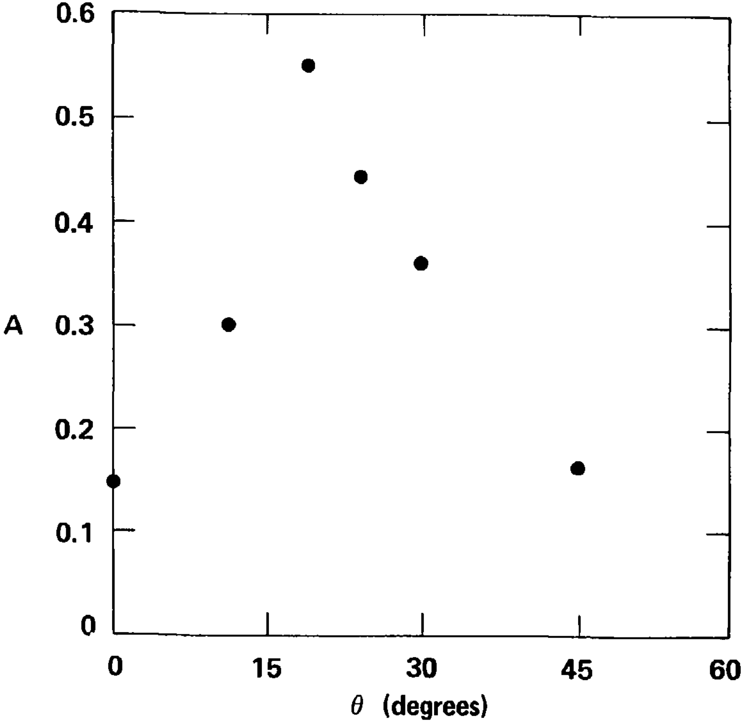

Fig. 12

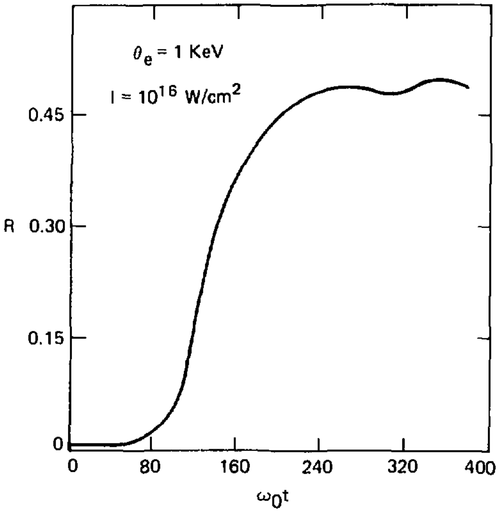

$\theta_e = 1$ KeV
$I = 10^{16}$ W/cm^2
R
0.45
0.30
0.15
0
0
80
160
240
320
400
$\omega_0 t$

Fig. 13

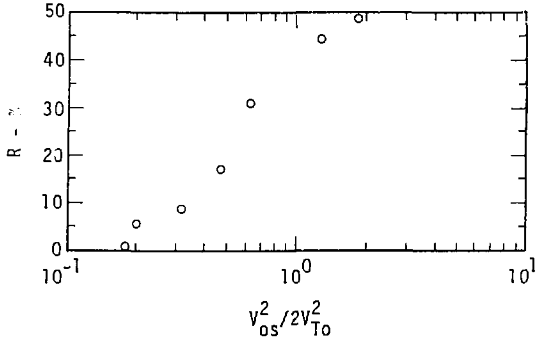

Fig. 14

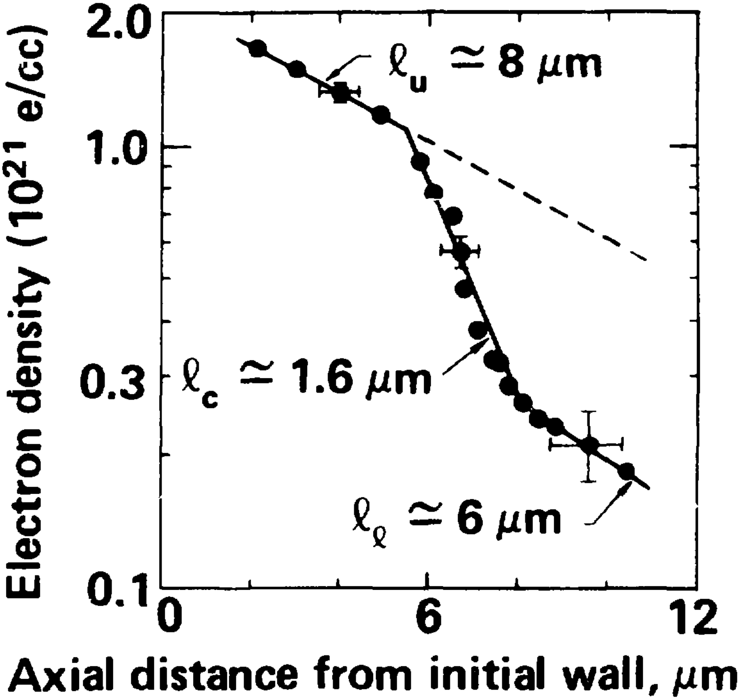
2.0
1.0
0.3
0.1
0
6
12
Electron density (10^{21} e/cc)
Axial distance from initial wall, μm
$\ell_u \simeq 8\ \mu m$
$\ell_c \simeq 1.6\ \mu m$
$\ell_\ell \simeq 6\ \mu m$

Fig. 15

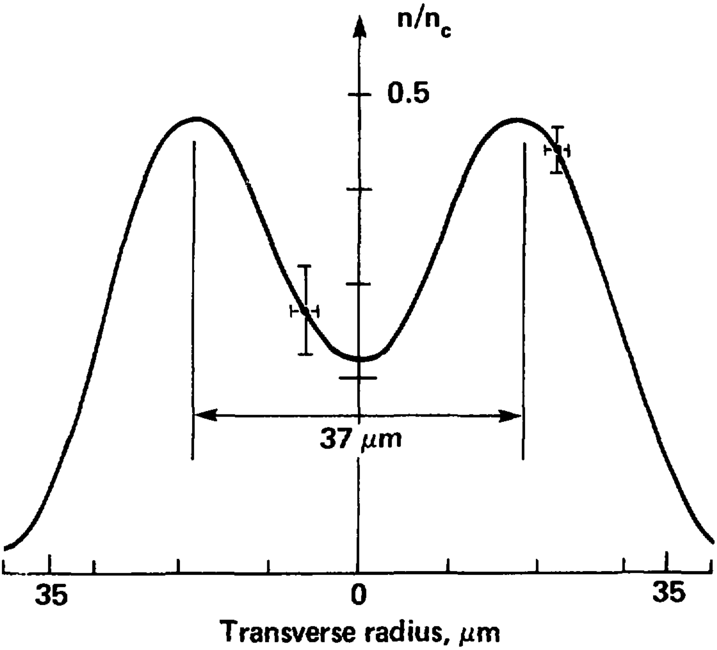

Fig. 16

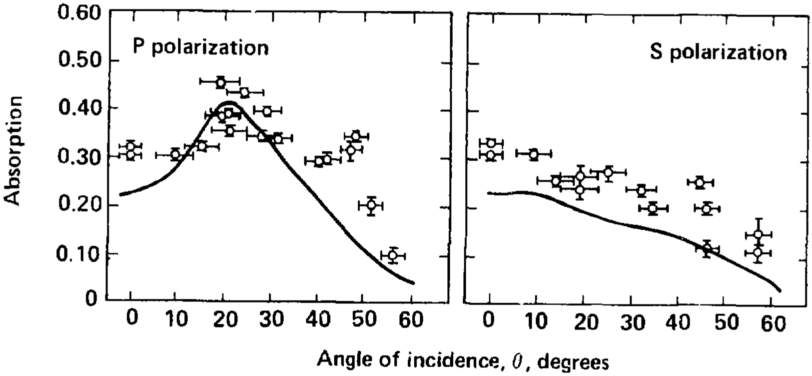
0.60
0.50
0.40
0.30
0.20
0.10
0
Absorption
P polarization
S polarization
0
10
20
30
40
50
60
Angle of incidence, θ, degrees

Fig. 17

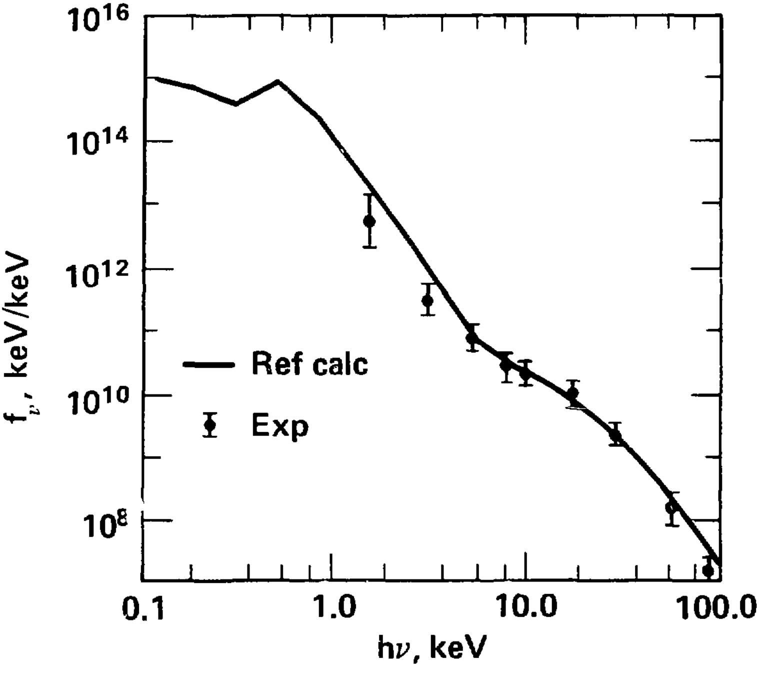

10^{16}
10^{14}
10^{12}
10^{10}
10^{8}
0.1
1.0
10.0
100.0
$h\nu$, keV
f_ν, keV/keV
Ref calc
Exp

Fig. 18

Fig. 19

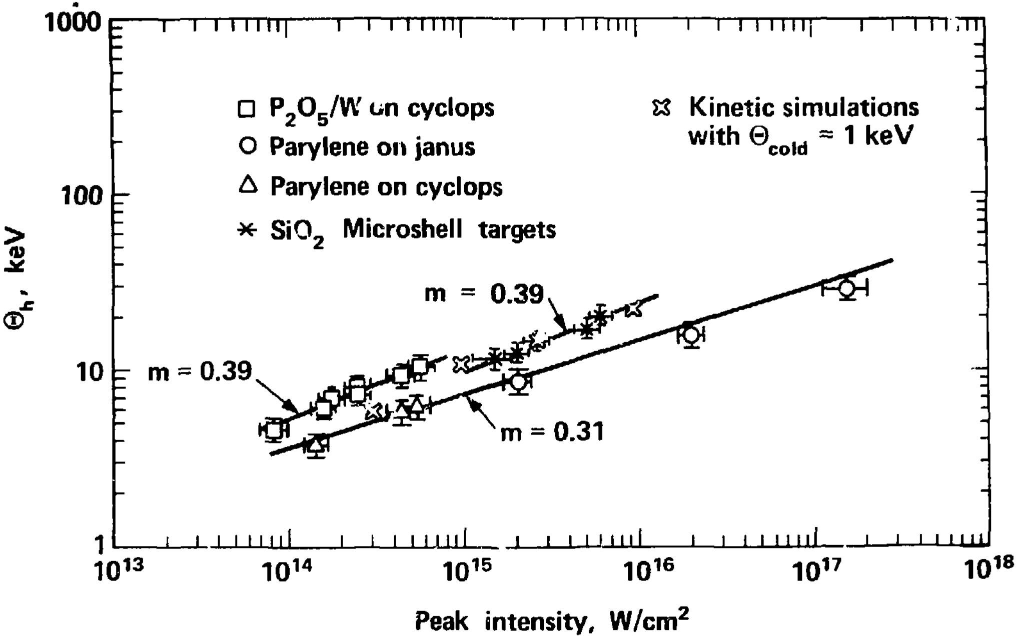
□ P_2O_5/W on cyclops
○ Parylene on janus
△ Parylene on cyclops
✳ SiO_2 Microshell targets
Kinetic simulations with $\Theta_{cold} \approx 1$ keV
m = 0.39
m = 0.39
m = 0.31
Θ_h, keV
1000
100
10
1
10^{13}
10^{14}
10^{15}
10^{16}
10^{17}
10^{18}
Peak intensity, W/cm^2

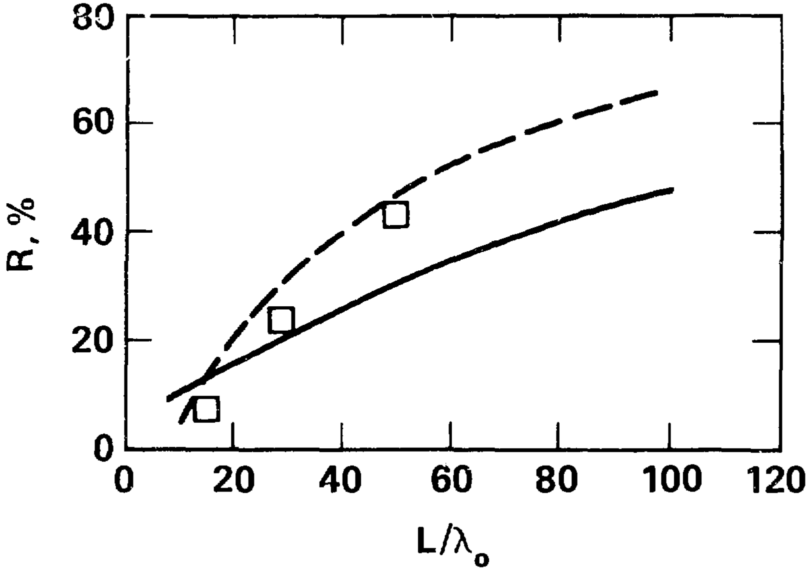

Fig. 20

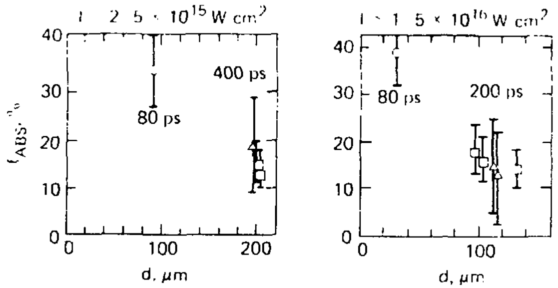
1 – 2.5 × 10^15 W cm^-2
400 ps
80 ps
f_ABS, %
40
30
20
10
0
0
100
200
d, μm
1 – 1.5 × 10^16 W cm^-2
80 ps
200 ps
40
30
20
10
0
0
100
d, μm

Fig. 21

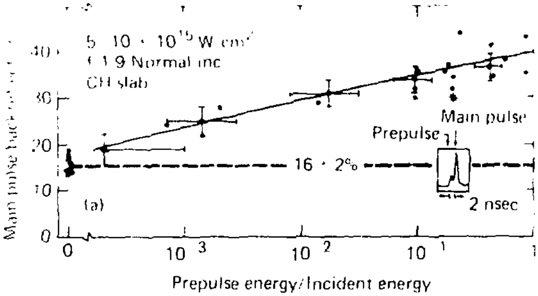
5 10 · 10^15 W cm^-2
f 1.9 Normal inc
CH slab
Main pulse back
40
30
20
10
0
(a)
16 · 2%
Prepulse
Main pulse
2 nsec
0
10^-3
10^-2
10^-1
1
Prepulse energy/Incident energy

Fig. 22

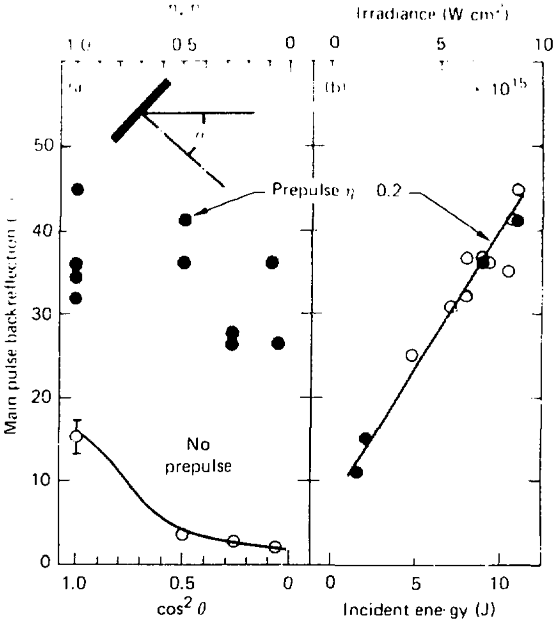
Irradiance (W cm⁻²)
1.0
0.5
0
0
5
10
(a)
(b)
× 10¹⁵
θ
Prepulse η 0.2
No prepulse
Main pulse backreflection (
50
40
30
20
10
0
1.0
0.5
0
0
5
10
cos² θ
Incident energy (J)

Fig. 23